SOILS AND FOUNDATIONS Vol. 47, No. 3, 473–491, June 2007
Japanese Geotechnical Society

RATE-DEPENDENT LOAD-STRAIN BEHAVIOUR OF GEOGRID ARRANGED IN SAND UNDER PLANE STRAIN COMPRESSION

WARAT KONGKITKUL[i], FUMIO TATSUOKA[ii] and DAIKI HIRAKAWA[iii]

ABSTRACT

A number of previous experimental studies showed that polymer geogrid reinforcement as well as sand exhibit significantly rate-dependent behaviour. The viscous properties of polymer geogrids and Toyoura sand were independently evaluated by changing stepwise the strain rate as well as performing sustained loading and load/stress relaxation tests during otherwise monotonic loading in, respectively, tensile loading tests and drained plane strain compression (PSC) tests. The viscous properties of the two types of material were separately formulated in the same framework of non-linear three-component rheology model. The viscous response of geogrid-reinforced sand in PSC is significant, controlled by viscous properties of geogrid and sand. Local strain distributions in the reinforced sand specimen were evaluated by photogrametric analysis and used to determine the time history of the tensile strain in the geogrid. The time history of tensile load activated in the geogrid during sustained loading of reinforced sand specimen was deduced by analysing the measured time history of geogrid strain by the non-linear three-component model. It was found that the tensile load in the geogrid reinforcement arranged in a sand specimen subjected to fixed boundary loads could decrease with time. In that case, the possibility of creep rupture of geogrid is very low.

Key words: creep deformation, geogrid-reinforced sand, load relaxation, plane strain compression, three-component model, viscous property (**IGC**: D6/K14)

INTRODUCTION

A great number of permanent geosynthetic-reinforced soil (GRS) structures have been constructed due to their high-cost effectiveness and high seismic stability in highly seismic zones, in particular (e.g., Tatsuoka et al., 1997). To predict their residual deformation by static sustained loads during service, the viscous properties of the backfill and geosynthetic reinforcement as well as their interactions should be properly understood. It is known that both geomaterial (i.e., soil and rock) and geosynthetic reinforcement exhibit significant rate-dependent (i.e., viscous) behaviours. This issue was studied by a great number of researchers, including Matsushita et al. (1999), Di Benedetto et al. (2002), Tatsuoka et al. (1999, 2002), Nawir et al. (2003) and Kiyota and Tatsuoka (2006) for granular materials, which are used as the backfill for most GRS structures, and by Hirakawa et al. (2003) and Kongkitkul et al. (2004, 2007a) for polymer geosynthetic reinforcements. However, the study on the viscous behaviour of geosynthetic-reinforced sand, which is very complicated due to interactions between the viscous properties of backfill and geosynthetic reinforcement, is very limited (e.g., Kongkitkul et al., 2007b).

In routine design, on the other hand, GRS structures are usually designed based on the limit-equilibrium stability analysis ignoring the rate-dependent deformation characteristics (e.g., creep deformation) of the backfill. The possibility of the creep rupture of geosynthetic reinforcement is taken into account by largely reducing the rupture tensile strength evaluated by fast tensile loading tests of virgin product using the so-called ''creep reduction factor'' (Fig. 1). Tatsuoka et al. (2004, 2006) argued that the possibility of creep rupture of geosynthetic reinforcement is overly taken into account in this routine design method (Fig. 1). Firstly, the creep reduction factor to render the tensile load by which the creep rupture would take place at the end of full design life is applied after having reduced the tensile strength by accounting for the full degradation effects that would have taken place by the end of design life. That is, the possibility of creep rupture of a geosynthetic reinforcement that has deteriorated by the end of the full design life is evaluated. The actual tensile load by which the creep rupture would take place at the end of full design life is in between the creep rupture strengths of the geosynthetic reinforcements before and after full degradation during the design life (Tatsuoka et al., 2006; Kongkitkul et al.,

[i] Postdoctoral Fellow, Department of Civil Engineering, Tokyo University of Science, Japan (formerly Graduate Student of the University of Tokyo, Japan).
[ii] Professor, Department of Civil Engineering, Tokyo University of Science, Japan (tatsuoka@rs.noda.tus.ac.jp).
[iii] Assistant Professor, ditto.
The manuscript for this paper was received for review on May 31, 2006; approved on January 15, 2007.
Written discussions on this paper should be submitted before January 1, 2008 to the Japanese Geotechnical Society, 4-38-2, Sengoku, Bunkyo-ku, Tokyo 112-0011, Japan. Upon request the closing date may be extended one month.

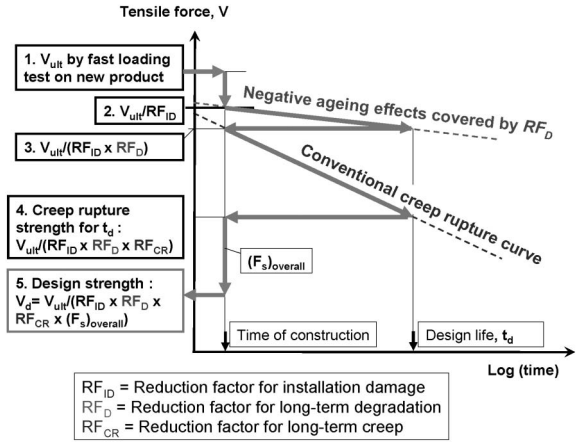

Fig. 1. Method that is popular in use to obtain the design tensile strength of geosynthetic reinforcement accounting for the possibility of creep rupture (after Tatsuoka et al., 2004, 2006)

2007c). Secondly, soil exhibits more-or-less creep deformation when subjected to sustained loading, which may result in creep failure under some conditions. It is a usual geotechnical engineering practice, however, to determine the design shear strength of soil without reducing by using the so-called creep reduction factor when creep failure is deemed to be certainly unlikely to take place. Rather, the effects of strain rate on the shear strength are taken into account when relevant (e.g., when dealing with soft clay). The design method illustrated in Fig. 1 is obviously different from this geotechnical engineering method described above. When following this geotechnical engineering method to determine the design rupture strength of geosynthetic reinforcement, in case the overall safety factor is larger than the actual creep reduction factor, which should be smaller than the creep reduction factor, RF_{CR}, determined by the conventional creep rupture curve (Fig. 1), the design rupture strength is determined without taking into account a creep reduction factor while taking into account the strain rate effects. Lastly, it is assumed in this design procedure (Fig. 1) that the tensile load mobilised in the geosynthetic reinforcement is maintained constant for the design life, despite that it is very likely that the tensile load could decrease with time due to the viscous compressive deformation in the lateral direction of the backfill and a kind of load relaxation phenomenon of geosynthetic reinforcement. This last point is the topic of this paper.

Most of the previous experimental studies to evaluate the effects of the stiffness, surface roughness and structure (i.e., shape, covering ratio (CR) and so on) of geosynthetic reinforcement and the backfill type on the deformation and strength characteristics of geosynthetic-reinforced soil were performed by means of plane strain compression (PSC) tests (e.g., Tatsuoka and Yamaguchi, 1986; Ling and Tatsuoka, 1994; Roh and Tatsuoka, 2002). Furthermore, numerical analysis of the issue mentioned above was performed mainly by the plane strain FEM (e.g., Kotake et al., 1999; Peng et al., 2000). A great number of scaled-down model tests were performed to evaluate the performance of GRS bridge abutment (e.g., Shinoda et al., 2003; Uchimura et al., 2003) and of GRS retaining wall (e.g., Hirakawa et al., 2004) as well as the bearing capacity of a shallow footing on geosynthetic-reinforced level ground and slope (e.g., Huang and Tatsuoka, 1990; Huang et al., 1994; Huang and Tatsuoka, 1994). To simulate most prevailing field conditions, most of these scaled-down model tests were performed under plane strain conditions. The corresponding numerical analysis was performed by the plane strain FEM (e.g., Kotake et al., 2001a, b, 2004). Three-dimensional FEM analysis of large deformation and failure of reinforced structure is very limited.

Another advantage of plane strain physical tests is that local strain distributions in the specimen can be determined by photogrametric analysis of digitised coordinates of the markers on a set of pictures of the σ_2-plane of specimen taken at different loading stages. A number of researches studied on strain localisation and bifurcation in a sand specimen subjected to drained PSC by this method, based on displacements of spaced markers (Stroud, 1971) or nodes of grids printed on the specimen membrane (e.g., Desrues, 1984; Yoshida et al., 1994; Yoshida and Tatsuoka, 1997; Liang et al., 1997; Alshibli and Sture, 2000).

In view of the above, a series of drained PSC tests were performed on air-dried Toyoura sand unreinforced or reinforced with two different types of polymer geogrid in the present study. Sustained loading (SL) tests were performed during otherwise monotonic loading (ML). Time histories of tensile strain of a geogrid reinforcement layer arranged in sand during sustained loading of reinforced sand specimen were evaluated by the photogrametric analysis. Then, with help of numerical simulation based on a non-linear three-component rheology model (described in this paper), the tensile load-tensile strain-time behaviour of geogrid was deduced to examine whether the tensile load of polymer geogrid is maintained constant or decreases with time during sustained loading of reinforced sand specimen.

TEST MATERIALS

Reinforced PSC specimens were prepared by using Toyoura sand, a sub-angular uniform fine quartz-rich sand. The particle size ranges from 75 to 260 μm with $D_{50} = 0.2$ mm; the maximum and minimum void ratio are 0.98 and 0.62; and the specific gravity is 2.65. Figure 2 shows the stress-strain behaviour of unreinforced Toyoura sand obtained from a drained PSC test performed by Kongkitkul et al. (2007b). The dimensions and preparation method of the specimen are the same as those employed to prepare the reinforced specimens, which are given later in this paper. A significant rate-dependency of stress-strain behaviour of Toyoura sand may be seen from: a) a stress ratio jump upon a step increase/decrease in the vertical strain rate; b) a vertical strain increment during sustained loading at a constant stress ratio; and c) stress ratio relaxation at a constant vertical strain. Di

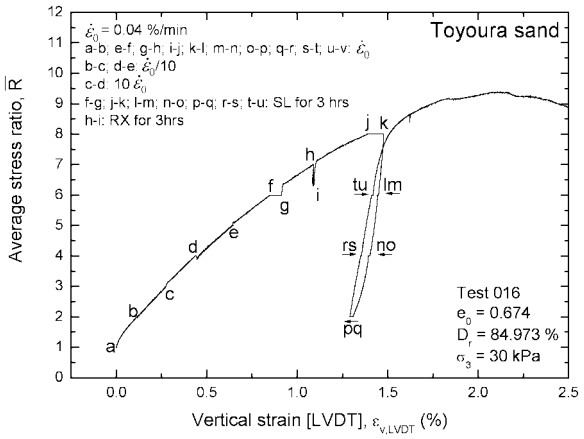

Fig. 2. $\bar{R}-\varepsilon_{v,LVDT}$ relation of unreinforced Toyoura sand (after Kongkitkul et al., 2007b)

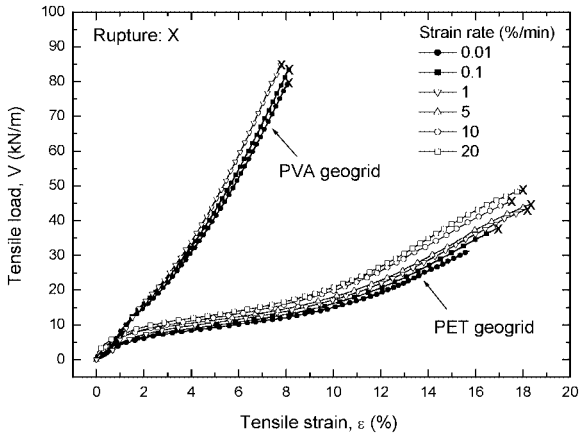

Fig. 4. Tensile load-strain relations from continuous ML at different but constant strain rates, PET and PVA geogrids (after Hirakawa et al., 2003)

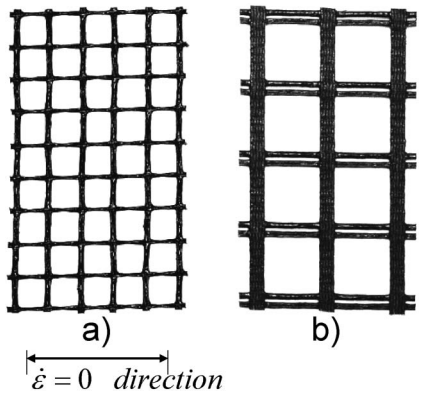

Fig. 3. Pictures of: a) Polyester (PET) geogrid; and b) Polyvinyl alcohol (PVA) geogrid used to reinforce PSC sand specimens

Benedetto et al. (2002) and Tatsuoka et al. (2002) argued on the possible mechanism for the viscous properties of sand.

Two types of polymer geogrid, provided by a Japanese manufacturer, were used (Fig. 3). The first one is a biaxial type of polyester (PET) geogrid. It has an average thickness of about 1 mm and a centre-to-centre spacing of 9 mm in both longitudinal and transverse directions with a covering ratio (CR) of 22.2%, coated with PVC resin for UV protection. This type of geogrid is relatively weak when compared with others used in the construction of prototype GRS structures while it has been used in a number of scaled-down model tests aiming at satisfying the similitude (e.g., Shinoda et al., 2002, 2003; Hirakawa et al., 2002). The other one is a single-axial type consisting of polyvinyl alcohol (PVA) fibre in both longitudinal and transverse directions with a thickness of 1 mm, a centre-to-centre spacing between two adjacent members of 20 mm in both longitudinal and transverse directions and a CR equal to 25%.

Figure 4 shows the tensile load-tensile strain relations of the PET and PVA geogrids from tensile loading tests performed by Hirakawa et al. (2003) and Kongkitkul et al. (2004). The rupture strengths at a strain rate of 1.0% min of the PET and PVA geogrids are 39.2 and 85.2 kN/m. Moreover, the secant stiffness at a tensile strain of 5% of the PET and PVA geogrids are 220 and 910 kN/m (when the strain rate is equal to 1.0%/min). These load-strain properties, which are highly non-linear and rate-dependent as seen from this figure, are basically elasto-viscoplastic.

TEST METHOD

Drained PSC Tests on Geogrid-reinforced Specimens

As the details of the test method are described in Kongkitkul et al. (2007b), only a brief description is given below. The reinforced specimens (Fig. 5(a)) were prepared by pluviating air-dried particles of Toyoura sand through air to obtain a target relative density of 85% (n.b., the measured relative density ranged from 84% to 88%). Two layers of either PET or PVA geogrid were placed at the levels of one forth and three forth of the specimen height. The surface of respective precedent sand layer was levelled and smoothened by means of a controlled vacuuming system before placing a geogrid layer. The top and bottom as well as lateral ends of the PSC specimens were well-lubricated. Confining pressure of 30 kPa was applied by partial vacuuming and measured by using a pressure transducer.

The average vertical and lateral stresses were measured with an axial load cell and another load cell equipped at the reacting lateral confining platen. External axial strains were obtained from compressions between the specimen cap and pedestal measured with a LVDT, while local axial strains were with a pair of LDTs (Fig. 5(a)). Only average axial strains measured by LVDT, $\varepsilon_{v,LVDT}$, are presented in this paper considering highly non-uniform deformation of the specimen due to tensile reinforcing effects. These externally measured axial strains, including bedding error effects, are not used in the analysis of the strain and load of geogrid. Horizontal strains were measured by using three pairs of proximity transducers located at the two levels of reinforcement layers to locally measure the average tensile strain of

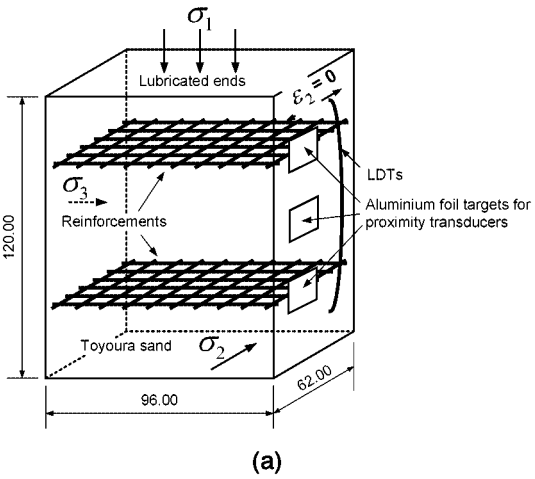

Fig. 5(a). Reinforced Toyoura sand specimen for PSC tests (unit: mm)

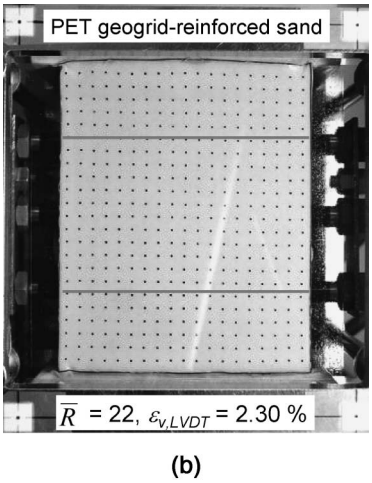

Fig. 5(b). σ_2-face of a reinforced PSC specimen with markers printed on the specimen's membrane (the two horizontal lines indicate the locations of geogrid)

geogrid and at the mid-height of specimen (Figs. 5(a) and (b)).

Markers, in total 23 and 19 in the vertical and horizontal directions with a centre-to-centre spacing of about 5 mm, were printed on the rubber membrane of specimen as seen from Fig. 5(b). A number of pictures of the specimen were taken through the front Acrylic confining platen during each PSC test for the photogrametric analysis explained later.

Loading System

The axial loading system, which has a capacity of about 50 kN, consists of a precise gear system with practically no backlash upon load reversal, operated by a computer-controlled servo-motor (Tatsuoka et al., 1994; Santucci de Magistris et al., 1999). By controlling the displacement to an accuracy of less than 1 μm in an automated way, it becomes possible to: a) smoothly switch between displacement and load control loading modes and between sustained loading or stress relaxation

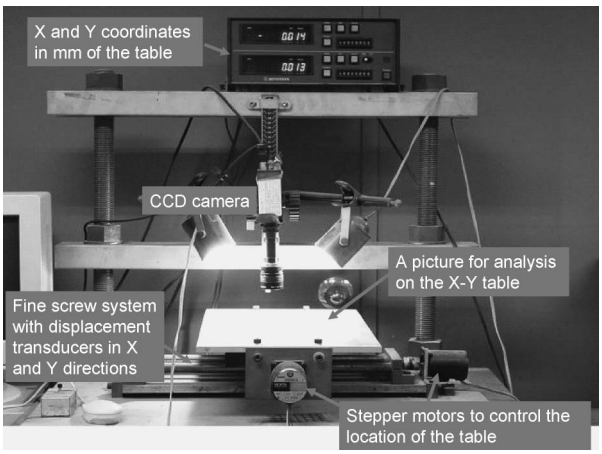

Fig. 6. Photogrametric system used to digitise the coordinates of markers on a picture (Yoshida et al., 1994; Yoshida and Tatsuoka, 1997)

stage and a constant strain rate loading or unloading phase; b) change the strain rate stepwise or gradually by a factor of up to 3,000; and c) apply very small amplitude unload/reload cycles to evaluate the elastic properties of test material during otherwise ML at a constant strain rate.

Digitising System for Specimen Deformation

The coordinates of the markers printed on the σ_2-face of the specimen membrane were automatically digitised to an accuracy of 0.03 mm or less by means of a digitising system (Fig. 6; Yoshida et al., 1994; Yoshida and Tatsuoka, 1997). It consists of: a) a movable XY table driven by two stepper motors having a precision of 1 μm; b) a microscope equipped with a Charge Coupled Device (CCD) camera; and c) computer software to determine the x- and y-coordinates at the geometric centre of each marker. The XY table was manually moved by using a pair of driving motors until each marker is located near the node of vertical and horizontal centre lines in the view of the microscope which was displayed on an auxiliary screen. Then, the coordinates at the geometric centre of the marker were digitised automatically by the computer software.

LOCAL STRAIN CALCULATION

In the present study, the iso-parametric formulation was used to calculate the strains in the respective element from the displacement vectors at the four nodes determined from the digitised coordinates. Four-node plane bilinear isoparametric elements were used to calculate the strains (Fig. 7). The details of the formulation are given in APPENDIX A. Figure 8 shows the algorithm used to obtain the coordinates of each four-node plane element and strains from changes in the nodal coordinates. The most basic element, close to a square of 5 mm × 5 mm, can be constructed from the four nodes located on the nearest vicinity of the respective element, which is hereinafter called ''the normal element''.

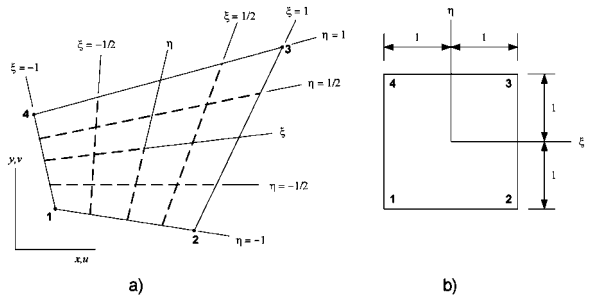

Fig. 7. Four-node plane bilinear isoparametric element in: a) *xy* space, and b) $\xi\eta$ space (after Cook et al., 1989)

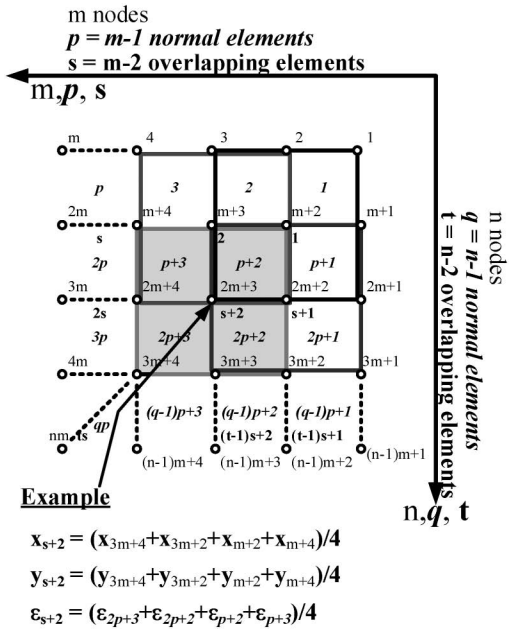

Fig. 8. Diagram showing the algorithm to obtain the coordinates of the respective formed element and its local strains

The accuracy of local strains depends on the accuracy of the nodal displacement scalars, u and v. The coordinates of the markers digitised in the present study were very accurate, as these quantities of respective single marker were determined by means of a microscope and this procedure was repeated with all the markers. Even by means of this digitising system, it was necessary to read as accurately as possible the coordinates of the nodes because of a relatively small size of the formed element. One of the possible sources of error in this local strain evaluation method is that it is sometimes difficult for the digitising system to accurately define the coordinates of exactly the same geometric centre of the respective marker with different shapes seen in different pictures taken after and before some deformation of specimen during the respective PSC test. This type of error becomes larger as the shape of marker changes largely due to large deformation of the specimen.

In order to reduce the errors in calculated local strains while scarifying the sharpness of local strain determination, a larger four-node overlapping element, each having square shape of about 10 mm × 10 mm, was implemented (Fig. 8). These larger elements were formed by overlapping the ''normal elements'' in both vertical and horizontal directions. Therefore, the numbers of overlapping element are $(23-2)=21$ and $(19-2)=17$ in the vertical and horizontal directions. The coordinates (x, y) of the four nodes of the respective large overlapping elements were obtained from the coordinates of the nodes forming the elements. For example, the coordinates (x, y) of the four nodes of the large overlapping element, 's + 2', are '3m + 4', '3m + 2', 'm + 2' and 'm + 4'. The local strains of the large overlapping elements were obtained as follows. Firstly the local strains for each normal element inside an overlapping element were calculated using changes in the coordinates of the four nodes forming each normal element. For example, the local strains in the normal element, 'p + 2' were calculated from changes in the four surrounding coordinates at the nodes: '2m + 3', '2m + 2', 'm + 2' and 'm + 3'. Then, the local strains in the large overlapping element was obtained by directly averaging the strains in the inside four ''normal elements''. For example, the local strains in the overlapping element, 's + 2', were obtained by directly averaging the local strains in the inside four ''normal elements'': '2p + 3', '2p + 2', 'p + 2' and 'p + 3'. In this way, the contours of strain became smoother and more natural than when based on the local strains of normal elements (Kongkitkul, 2004).

Table 1. List of test name with the respective geogrid types and sustained loading levels

Test name	Geogrid type	$\bar{R}$	Period of sustained loading
Test 041	PET	16.67	30 days
Test 008	PET	26.67	15 hours
Test 028	PVA	26	24 hours

TEST RESULTS AND NUMERICAL ANALYSIS

As the axial stress, σ_1, acting on the top and bottom ends of a reinforced specimen is not uniform due to the tensile reinforcing effects, the average stress states in the reinforced sand specimens are expressed in terms of the average stress ratio, $\bar{R}=\bar{\sigma}_z/\sigma_c$, where $\bar{\sigma}_z$ is the average vertical stress; and σ_c is the confining pressure (30 kPa). In the following, the results from the three PSC tests on reinforced Toyoura sand listed in Table 1 are presented. In this table, the values of $\bar{R}$ denote the stress levels where the geogrid load-strain-time behaviour was analysed.

Sustained Loading Test on a PET Geogrid for 30 Days (Test 041)

First the tensile load-strain-time behaviour of a PET geogrid arranged in Toyoura sand during sustained loading of a PET geogrid-reinforced Toyoura sand when the failure of reinforced sand is not imminent in test 041 is analysed.

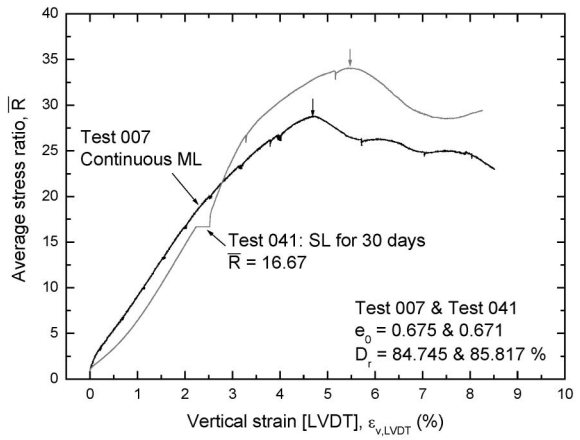

Fig. 9. $\bar{R}-\varepsilon_{v,LVDT}$ relations from PSC tests on reinforced Toyoura sand with a 30 day-long sustained loading stage (test 041) and small unload/reload cycles (test 007)

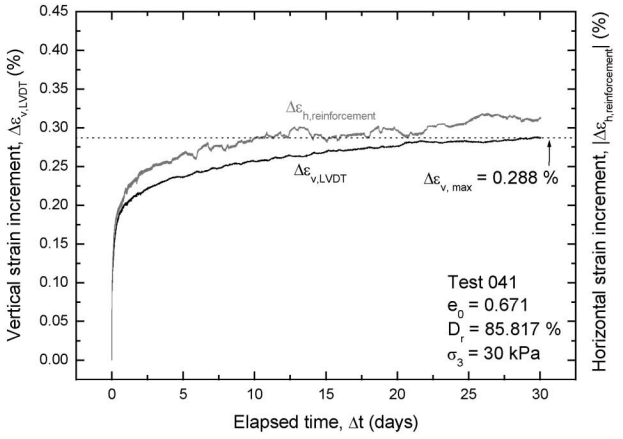

Fig. 11. Time histories of average vertical and horizontal strain increments of PET geogrid-reinforced sand PSC specimen during 30 day-long sustained loading

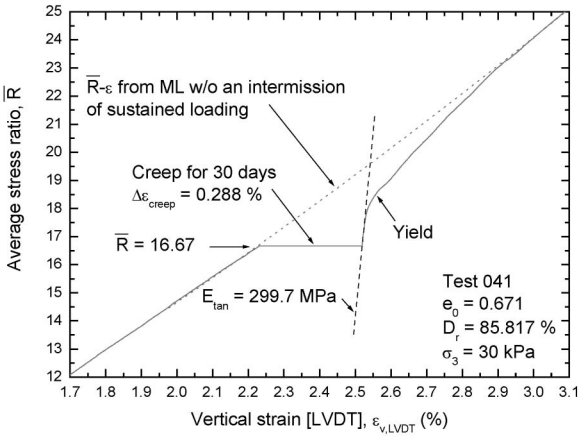

Fig. 10. Close-up of $\bar{R}-\varepsilon_{v,LVDT}$ relation immediately before, during and immediately after a sustained loading stage presented in Fig. 9

Stress-strain Behaviours of Reinforced Sand Specimen

Figure 9 shows the relationships between the average stress ratio, $\bar{R}$, and the average vertical strain, $\varepsilon_{v,LVDT}$, from test 041 on a PET geogrid-reinforced sand specimen, in which sustained loading was performed for 30 days at $\bar{R}=16.67$, about a half of the peak strength. For reference, the relation from a continuous ML test with several small unload/reload cycles (test 007) is also presented. The vertical (axial) strain rate during ML was 0.04%/min in the two tests. A noticeable discrepancy may be seen between the two stress-strain relations. This discrepancy is due mostly to differences in the tangent modulus when the vertical strain is less than about 0.5% between the two tests, which can be attributed to different effects on the two stress-strain relations of bedding errors at the interface between the geogrid and the adjacent sand part, as described in detail by Kongkitkul et al. (2007b). Figure 10 is a close-up immediately before, during and immediately after 30 day-long sustained loading from test 041. Figure 11 shows the time histories of vertical strain increment (averaged for the whole specimen height) and horizontal strain increment (average of those at the two levels of reinforcement layers measured with two pairs of proximity transducers, Fig. 5(a)) during the sustained loading for 30 days. The following trend of behaviour may be seen:

1) Significant creep deformation takes place during the 30 day-long sustained loading, which should be due to not only the viscous properties of PET geogrid but also those of Toyoura sand.
2) The creep strain rate decreases at a large rate with an increase in the elapsed time at the initial stage while the rate at an elapsed time of 30 days is very small. About 70% of the total creep strain observed at an elapsed time of 30 days has developed during the first one day. Moreover, the average vertical strain of the reinforced sand specimen at an elapsed time of 30 days is still about a half of the value at the ultimate failure. From these facts, it is unlikely that the creep failure of the reinforced sand specimen is imminent at the end of this sustained loading.
3) The $\bar{R}-\varepsilon_{v,LVDT}$ relation exhibits a very high stiffness upon the restart of ML following the sustained loading. Then, unlike unreinforced sand (Fig. 2), the relation exhibits a clear yield point at a stress level that is noticeably lower than the relation obtained from continuous ML at the same strain rate without an intermission of sustained loading (Fig. 10). This trend of behaviour suggests that the tensile load mobilised in the PET geogrid decreased during the 30 day-long sustained loading, which resulted into a decrease in the confining pressure exerted on the sand part, thereby a decrease in the yield stress. This point is discussed in detail later in this paper.
4) During subsequent ML towards the ultimate failure, the reinforced sand becomes even stiffer and stronger than when not subjected to this sustained loading (Fig. 9). This improvement of stress-strain behaviour by sustained loading is due likely to a better interlocking between the geogrid and the adjacent sand that developed during the 30 day-long sustained loading.

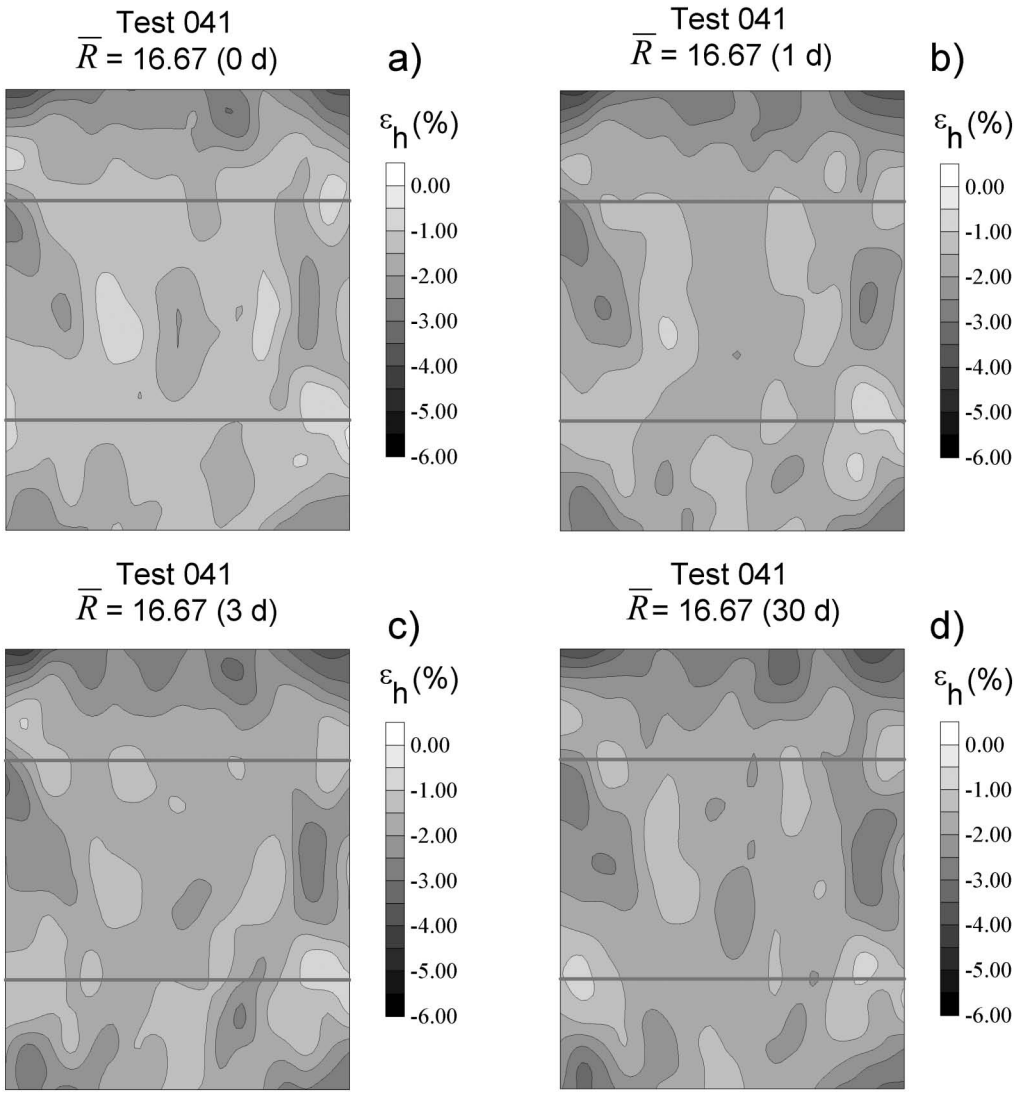

Fig. 12. Local horizontal strain contours from a 30 day-long sustained loading test at $\bar{R} = 16.67$: a) at the start of sustained loading; and after: b) 1 day, c) 3 days, and d) 30 days, test 041; the two horizontal lines indicate the initial locations of the two layers of reinforcement

These facts 3) and 4) indicate that creep deformation of reinforced sand is not a degrading phenomenon, but it is merely an interacting viscous response of sand and geogrid.

Time History of Strain in the Geogrid Arranged in Sand

Figure 12 show the local horizontal strain fields at the start of, as well as at elapsed times of 1 day, 3 days and 30 days during, the sustained loading at $\bar{R} = 16.67$ obtained by the photogrametric analysis. The strains are defined zero at the start of PSC loading. It may be seen that the local horizontal strains around the PET geogrid layers are noticeably smaller than those in the adjacent zones (not including a geogrid). This result shows the restraining effects of the geogrid. As it was not possible to reliably evaluate the distribution of local strain along the respective geogrid layers, the tensile strains of the PET geogrid averaged for the whole length (excluding 3 mm at each end) at different elapsed times were obtained by assuming that they are the same as the average horizontal strains in the respective 1 cm-thick horizontal band including a geogrid layer. This assumption is relevant as any slippage between the geogrid and the adjacent sand is unlikely to have taken place. The data points presented in Fig. 13 represent these average geogrid strains obtained as above.

It was also assumed that the average lateral strain of a reinforced sand specimen measured with proximity transducers set at the geogrid levels (Fig. 5(a)) is the same as the average geogrid strain. In Fig. 13, the continuous time history of average geogrid strain obtained based on this assumption (before scaling) is also plotted. This time history of geogrid strain is similar to the one obtained by the photogrametric analysis. Despite that the geogrid strains obtained by the photogrametric analysis are more representative of the geogrid strains than those obtained by the proximity transducer measurement, the number of the data points is not sufficient to accurately deduce a continuous time history. Therefore, combining the results by the two methods, the continuous time history of average geogrid tensile strain was obtained: i.e., the time history from the proximity transducer measurement

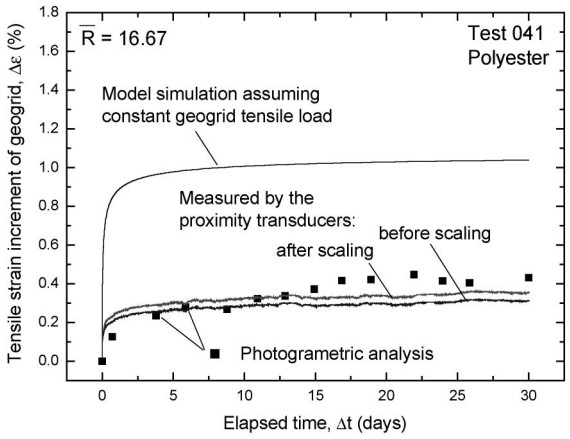

Fig. 13. Comparison among the time histories of average tensile strain in the PET geogrid obtained by photogrametric analysis, proximity transducer measurements (before and after scaling) and model simulation assuming a constant tensile load

was scaled in the vertical direction to be fitted to the data points obtained by the photogrametric analysis (Fig. 13). This continuous time history of PET geogrid tensile strain (after scaling) is used to estimate the time history of the tensile load in the geogrid. The time history of average tensile strain increment obtained by model simulation assuming constant tensile load shown in Fig. 13 is explained later.

As seen from Fig. 13, the continuous time history of average tensile strain of the PET geogrid arranged in sand during the sustained loading of the PSC specimen (after scaling) is not yet smooth enough to obtain stable and reliable values of strain and strain rate at a given elapsed time. For this reason, the measured time history was fitted by an empirical equation (or equations). As the entire measured time history of geogrid strain can not be satisfactorily fitted by a single equation, a segmental polynomial fitting method (Kongkitkul et al., 2007a) was used. That is, the measured relation were separated into three consecutive segments and fitted by three different equations having the following same three-degree polynomial form:

$$\Delta\varepsilon = A + B\cdot\log(\Delta t) + C\cdot[\log(\Delta t)]^2 + D\cdot[\log(\Delta t)]^3 \quad (1)$$

where $\Delta\varepsilon$ = geogrid strain increment (%); Δt = elapsed time (sec); and A, B, C and D = constants for each segment of time history, as listed in Table 2.

Figures 14(a), (b) and (c) show the results of this fitting procedure. It may be seen that the entire measured time history of strain of the PET geogrid during the sustained loading of PSC specimen is fitted very well by this segmental polynomial fitting method. Figure 15 (in the full-log plot) shows the time history of geogrid strain rate during the sustained loading for 30 days of the reinforced sand specimen obtained from the strain-time relation fitted by Eq. (1). It may be seen that the geogrid strain rate decreases at a large rate with elapsed time, becoming extremely small at an elapsed time of 30 days. It may also be seen that, except for the initial part (i.e., when Δt is

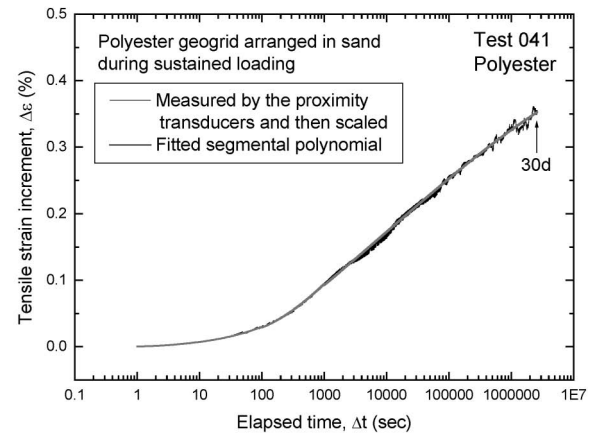

a)

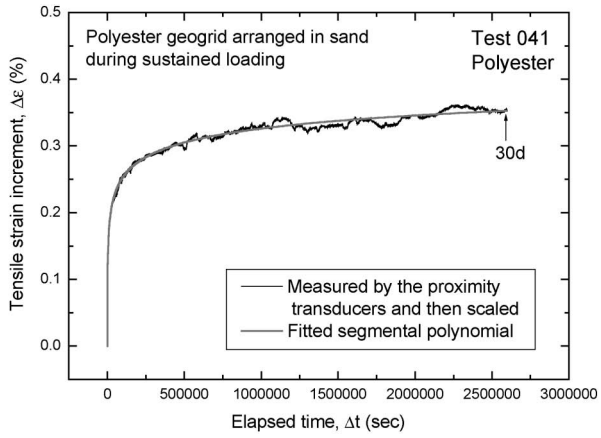

b)

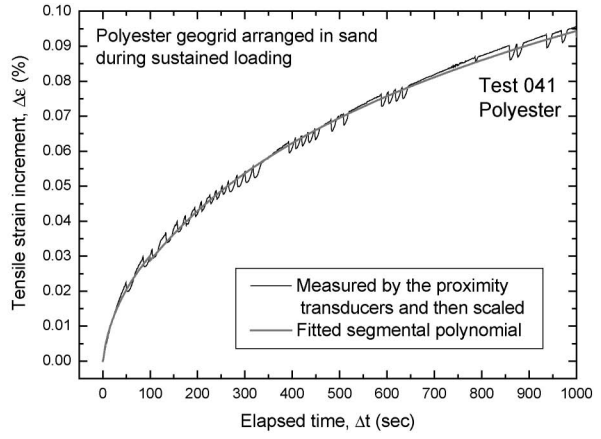

c)

Fig. 14. Time history of the strain increment of PET geogrid arranged in sand during sustained loading of the PSC specimen and its fitted relation: a) semi-log scale, b) arithmetic scale and c) close-up of Fig. 14(b) for the elapsed time from 0 to 1,000 seconds

shorter than about 500 seconds), the relation is rather linear in the full-log plot. When extrapolating this linear relation to an elapsed time of 50 years, a geogrid strain rate equal to 1.23×10^{-11}%/s is obtained, this is essentially negligible. This analysis also indicates that the creep rupture of this geogrid is not likely within the design life

Table 2. List of the constants in Eq. (1) for each segment of the time history of geogrid strain

Segment No.	Range of elapsed time (sec)	*A*	*B*	*C*	*D*
1	$0 \le \Delta t < 100$	−1.06E-03	7.76E-03	−2.91E-03	3.41E-03
2	$100 \le \Delta t < 1000$	1.3839E-01	−1.7059E-01	6.97E-02	−5.91E-03
3	$1000 \le \Delta t < 2592000$	−8.015E-02	2.719E-02	1.353E-02	−1.13E-03

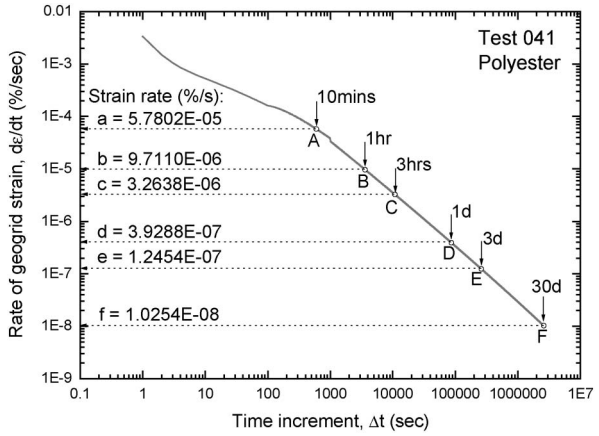

Fig. 15. Relationship between geogrid strain rate and elapsed time from the fitted time history of strain increment of PET geogrid arranged in sand during sustained loading of reinforced sand specimen (full-log plot)

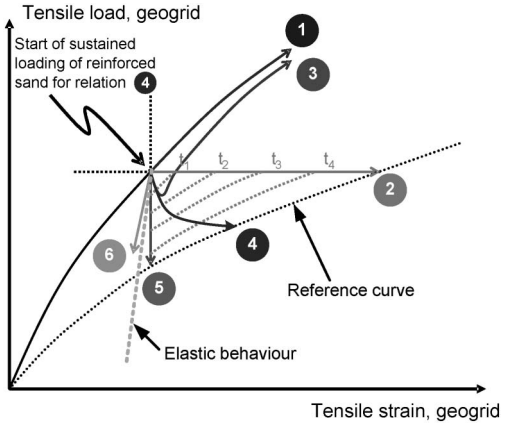

Fig. 16. Schematic diagram of tensile load-tensile strain relations for different loading histories of polymer geogrid reinforcement

of ordinary GRS structures, say 50 years.

Prediction of Tensile Load-strain Relation of Geogrid Arranged in Sand

Figure 16 illustrates the tensile load-strain relations (*1* through *6*) of a geogrid having viscous properties when subjected to the following different loading histories starting from a common state that has been reached by the same continuous ML at a constant strain rate:

Relation *1*: Continuation of ML at the same constant strain rate toward the ultimate failure.

Relation *2*: Sustained loading at a fixed load, as implicitly assumed in the conventional design of GRS structures (Fig. 1).

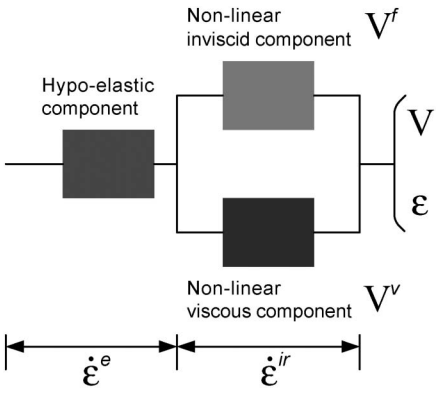

Fig. 17. Non-linear three-component model for geosynthetic reinforcement (Hirakawa et al., 2003; Kongkitkul et al., 2007a)

Relation *3*: Continuation of ML after a step decrease in the strain rate.

Relation *4*: The tensile load decreases with time at a decreasing rate while the strain rate decreases with time.

Relation *5*: Relaxation of the tensile load at a fixed strain.

Relation *6*: Unloading at a negative constant strain rate.

It is shown below that, when the failure of reinforced sand specimen is not imminent, relation *4* is relevant to the geogrid reinforcement arranged in sand during sustained loading of a reinforced sand specimen, while relation *2* largely over-estimates the residual strain in the geogrid. In Fig. 16, the contours for the identical elapse times since the start of these different loading histories are depicted. These contours are approximately valid only for stress-strain curves radiating from the same origin with the strain rate decreasing with time, like the curves 2, 4 and 5. On the other hand, these contours are not valid to stress-strain relations for which the strain rate is changed stepwise (e.g., curve *3*), or unloading in the sense that the irreversible strain rate is set to be negative is involved (e.g., curve *6*).

By knowing the time history of geogrid tensile strain evaluated as described above, the time history of tensile load mobilised in the geogrid, thus the relationship between the tensile load and the tensile strain of the geogrid during ML and subsequent sustained loading of a reinforced sand specimen can be obtained by numerical simulation based on a non-linear three-component model (Fig. 17; Hirakawa et al., 2003; Kongkitkul et al., 2007a). The structure of the model is described in APPENDIX B. Hirakawa et al. (2003) and Kongkitkul et al. (2004)

Table 3. List of parameters used in the non-linear three-component model simulation

Geogrid type	Combined parameter	Viscosity: $g_{v1}(\dot{\varepsilon}^{ir})$			Viscosity: $g_{v2}(\dot{\varepsilon}^{ir})$			Decay function			
	λ^v	α	m	$\dot{\varepsilon}^{ir}_r$	α^*	$1+b^*$	$\dot{\varepsilon}^{ir}_0$	r_i	r_f	c	n
PET	0.80	0.70	0.12	10^{-4}%/s	0.20	0.32	10^{-3}%/s	1.00	0.15	0.40	0.60
PVA	1.0	0.76	0.12	10^{-4}%/s	0.23	0.25	10^{-3}%/s	—	—	—	—

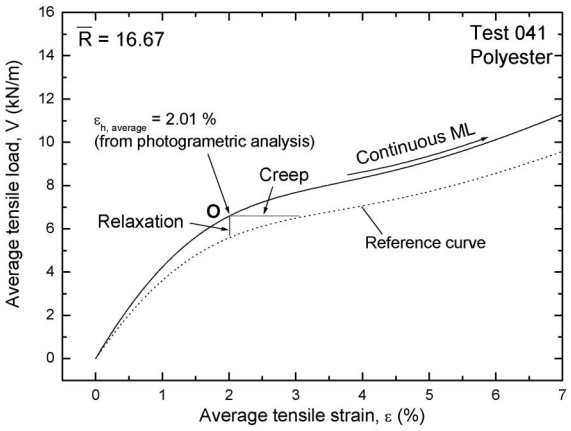

Fig. 18. Tensile load-tensile strain relations of a PET geogrid subjected to three specific loading histories: continuous ML, 30-day creep; and 30-day load relaxation, obtained by model simulation for sustained loading of reinforced sand specimen at $\bar{R}=16.67$ (Fig. 9)

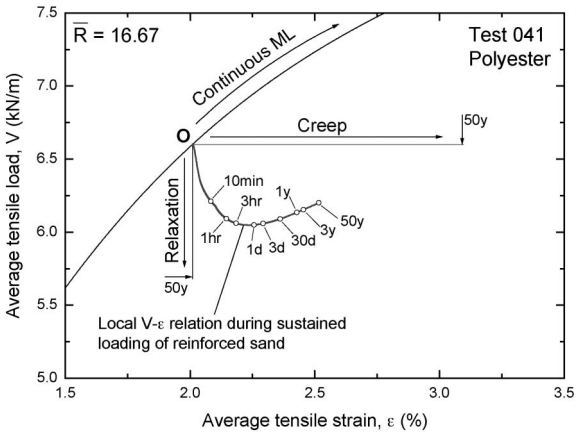

Fig. 19. Tensile load-tensile strain relation of a PET geogrid during the 30 day-long sustained loading of reinforced sand obtained by direct model simulation based on the time history of geogrid strain rate presented in Fig. 15

showed that the viscous property of PVA geogrid is of isotach type, for which the current viscous component of tensile load, V^v, is a unique function of instantaneous irreversible tensile strain and its rate, ε^{ir} and $\dot{\varepsilon}^{ir}$. On the other hand, the viscous property of PET geogrid is of combined type, for which V^v consists of the isotach component and the general TESRA component. A given increment of the latter component that has taken place at a certain moment, dV^v, decays with an increase in ε^{ir} while the decay rate increases with an increase in ε^{ir}. The details are explained in APPENDIX B. The simulation method based on the non-linear three-component model is explained in APPENDIX C. When simulating the rate-dependent load-strain behaviour of a geogrid, the interaction between the geogrid and the sand was modelled directly in the sense that the sand particles in contact with a geogrid layer move or deform together with the geogrid without slipping at the interface between them.

The time history of tensile load averaged for the whole length (excluding 3 mm at both ends) of the PET geogrid arranged in a PSC sand specimen was deduced by the method described above. It was not possible to reliably evaluate time-dependent changes in the non-uniform distribution of tensile force in the geogrid. FEM analysis is necessary to simulate this behaviour, which is beyond the scope of this paper and will be reported in the near future by the authors.

Figure 18 shows the tensile load-tensile strain relations of the PET geogrid for the following three loading histories obtained by simulations based on the non-linear three-component model:

1. Continuous ML at a tensile strain rate of 0.05%/min. This strain rate was determined from an increment of average geogrid strain obtained by the photogrametric analysis for an increase of $\bar{R}$ from 13.33 to 16.67 during the ML PSC test on reinforced Toyoura sand.
2. Sustained loading at a fixed tensile load lasting for 30 days that starts from point **O**. At point **O**, the stress-strain state of the reinforced specimen in the PSC test is $\bar{R}=16.67$ and the average tensile strain of the geogrid, $\varepsilon_{h,average}$, obtained by the photogrametric method (Fig. 12(a)) = 2.01%.
3. Load relaxation at a fixed strain lasting for 30 days starting from point **O**.

The model parameters used in these simulations are listed in Table 3 (Kongkitkul et al., 2007a).

The time history of the geogrid tensile strain for loading history 2 above is presented in Fig. 13. It can be readily seen from Fig. 13 that the tensile strain increment of the geogrid placed in sand measured during the sustained loading of the reinforced sand specimen is substantially smaller than the one obtained by model simulation assuming constant geogrid tensile load (i.e., loading history 2). This comparison indicates that the tensile load mobilised in the geogrid reinforcement arranged in sand decreases with time during sustained loading of the reinforced sand specimen.

Direct model simulation: Figure 19 shows a close-up

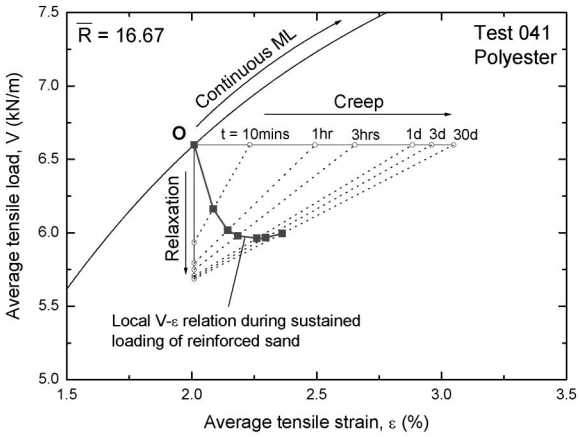

Fig. 20. Tensile load-tensile strain relation of a PET geogrid during the 30 day-long sustained loading of reinforced sand deduced based on linear contours constructed based on the behaviours during sustained loading and load relaxation

of Fig. 18. Based on the measured time history of geogrid strain rate during the 30 day-long sustained loading of the reinforced sand specimen starting from point **O** (presented in Fig. 15), the tensile load-strain-time relation of the PET geogrid was directly obtained by the non-linear three-component model simulation. The result is presented in Fig. 19. The direct model simulation was continued not only until an elapsed time of 30 days (as in the experiment) but also until an elapsed time equal to 50 years by extrapolating the linear relationship between the geogrid strain rate and the elapsed time presented in Fig. 15.

Despite that the direct model simulation shown above is the most direct means to deduce the time history of geogrid tensile load, the internal structure of this back analysis is difficult to readily understand. For this reason, the following several simplified procedures, which are less direct but much easier to understand, were attempted.

Linear contour assumption: As shown in Fig. 20, it was assumed that the contours for elapsed times equal to 10 minutes; 1 hour; 3 hours, 1 day, 3 days and 30 days be linear when applied to stress-strain relations radiating from point **O**. These contours of the PET geogrid were obtained based on the tensile load-tensile strain-time relations during sustained loading at a fixed tensile load and load relaxation at a fixed strain starting from point **O** obtained by model simulations. The tensile load-tensile strain relation of the PET geogrid arranged in sand during the sustained loading of reinforced sand specimen was then deduced by substituting the measured tensile strains of the PET geogrid at the specific elapsed times shown above, which is equal to the tensile strain at point **O** plus the tensile strain increment for the respective elapsed time obtained from the fitted time history of strain in Fig. 14, into these linear contours.

Elastic spring-support model: Considering that the actual contours for the same elapsed times may not be linear, they were obtained also by another method shown below. During load relaxation of a geogrid specimen, the total strain of the geogrid is kept constant. This situation

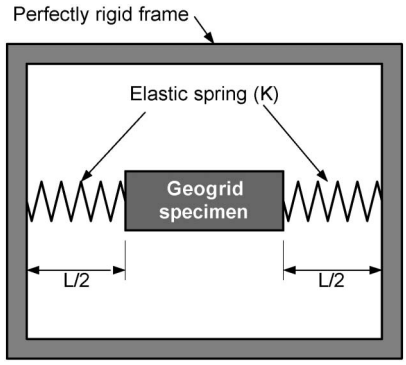

Fig. 21. Elastic spring-support model to express the behaviour of a geogrid specimen during sustained loading and load relaxation and intermediate behaviours

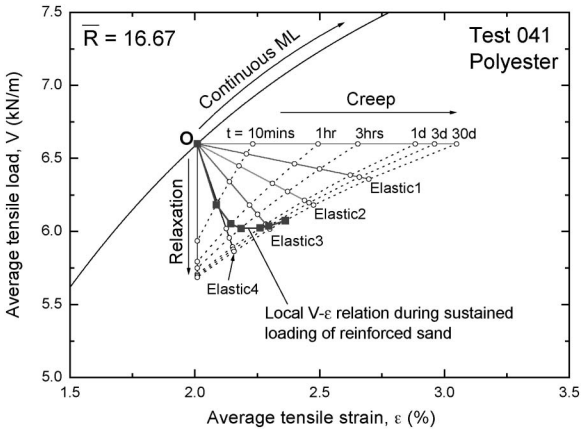

Fig. 22. Tensile load-strain relation of a PET geogrid during sustained loading of a reinforced sand specimen obtained based on the contours obtained by the elastic spring-support model

can be represented by a geogrid specimen in tension that is connected to a rigid frame via a pair of elastic spring with an infinitively large value of the spring constant, K (defined as the tensile force increment per change in the spring length: Fig. 21). In this case, the tensile load in the geogrid specimen decreases with time under the condition that $d\varepsilon =$ ''elastic tensile strain increment, $d\varepsilon^{e}(<0$: compressive)'' + ''irreversible tensile strain increment, $d\varepsilon^{ir}(>0$: tensile)'' $= 0$. On the other hand, sustained loading of the geogrid specimen can be represented by this model having zero spring constant, which can be realised by making the spring length infinitive without changing the spring structure per length. In this case, the tensile load in the geogrid specimen is kept constant with time under the condition that $d\varepsilon(>0) = d\varepsilon^{e}(=0) + d\varepsilon^{ir}(>0)$. The behaviour of a geogrid arranged in sand during sustained loading of reinforced sand specimen is intermediate between the behaviours during sustained loading and load relaxation simulated by the elastic spring-support model as described above. Therefore, this intermediate behaviour can be simulated by setting the spring constant between zero and infinitive. In this case, the tensile load in the geogrid specimen decreases with time under the condition that $d\varepsilon(>0) = d\varepsilon^{e}(<0) + d\varepsilon^{ir}(>0)$.

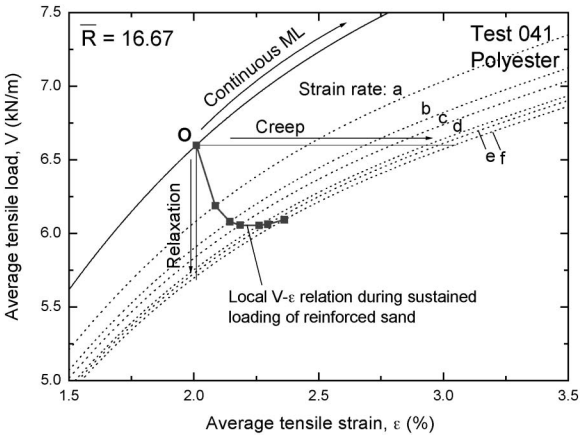

Fig. 23. Tensile load-strain relation of a PET geogrid during sustained loading of a reinforced sand specimen obtained based on the contours obtained by the isotach curve method

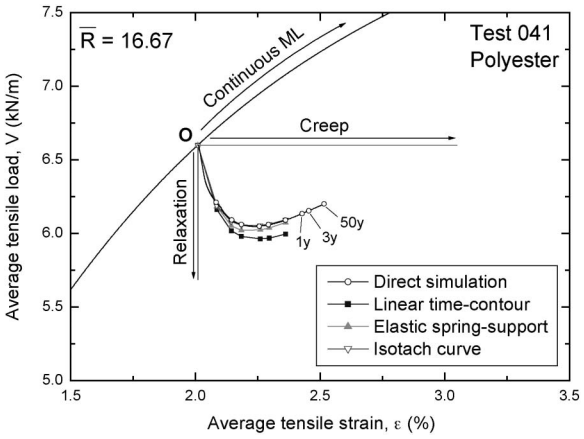

Fig. 24. Comparison of tensile load-strain relations of a PET geogrid arranged in sand during sustained loading of reinforced sand specimen obtained by the direct model simulation: the linear contour assumption, the elastic spring-support model, and the isotach curve

Figure 22 shows the tensile load-strain relations of the PET geogrid subjected to sustained loading and load relaxation as well as four radiating relations for the intermediate behaviours generated by model simulations using different spring constants, Elastic1 to Elastic4, all starting from point **O**. Then, segmental-linear contours at the elapsed times equal to 10 minutes; 1 hour; 3 hours, 1 day, 3 days and 30 days were obtained by connecting the points at the respective elapsed times along these relations. It may be seen that the contours are nearly linear when the elapsed time is small while it becomes slightly curved as the elapsed time becomes longer. The load–strain relation of the PET geogrid arranged in sand during the sustained loading of reinforced sand specimen was obtained by substituting the strains of PET geogrid measured at the respective elapsed times into these contours.

Isotach curves: When the viscosity is of isotach type, the current tensile load is a function of instantaneous irreversible tensile strain and its rate (APPENDIX B). Then, the tensile load–strain relation of a given geogrid for a given time history of irreversible strain rate can be deduced based on a set of isotach curves as shown in Fig. 23. Despite that the viscous property of the PET geogrid is of combined type, the isotach component is dominant. Therefore, it was attempted to obtain the tensile load–strain relation of the PET geogrid during the sustained loading of reinforced sand specimen based on the isotach curves (explained below).

The irreversible strain rates of the PET geogrid at elapsed times of 10 minutes, 1 hour, 3 hours, 1 day, 3 days and 30 days were read from the strain rate-time curve presented in Fig. 15 (points A, B, C, D, E and F). These strain rates are nearly the same as the respective irreversible strain rates in this case. Then, the isotach curves (i.e., the tensile load-strain relations) for these irreversible strain rates were generated by model simulation (i.e., a, b, c, d, e and f in Fig. 23). By knowing the time histories of irreversible strain and its rate, the load-strain relation of the PET geogrid arranged in sand during the sustained loading of reinforced sand specimen was then obtained by substituting them into the isotach curves.

Summary: Figure 24 compares the tensile load-strain relations of the PET geogrid arranged in sand during the 30 day-long sustained loading of reinforced sand specimen at $\bar{R} = 16.67$ obtained by the direct model simulation and the three simplified methods described above (Figs. 19, 20, 22 and 23). It may be seen that these results are nearly the same; in particular, the results from the direct simulation and the Isotach method are nearly fully overlapped. These results also show that the elastic-spring model, by which the actual behaviour of a geogrid arranged in sand can be easily captured, is relevant. It is also the case with another test as shown later in this paper. It may also be seen that, during the 30 day-long sustained loading of reinforced sand specimen, the tensile load in the PET geogrid first decreases significantly with time and then becomes rather constant. The geogrid tensile load then starts increasing. However, the increasing rate is very small. According to the model simulation, the geogrid tensile load would be kept significantly lower than the initial value even after an elapsed time of 50 years.

This result suggests that it is likely that the tensile load in the geosynthetic reinforcement arranged in the backfill of an ordinary GRS soil structure under static working loads also decreases with time. In that case, creep rupture failure of geosynthetic reinforcement is usually unlikely by the end of design life. Therefore, it might be conservative, perhaps overly, to assume that the tensile load in the geosynthetic reinforcement arranged in the backfill of a GRS soil structure under static working loads is kept constant during long-term sustained loading conditions of the structure. Tatsuoka et al. (2004, 2006) and Kongkitkul et al. (2007c) proposed a new method to determine the design rupture strength of geosynthetic reinforcement by not using a creep reduction factor.

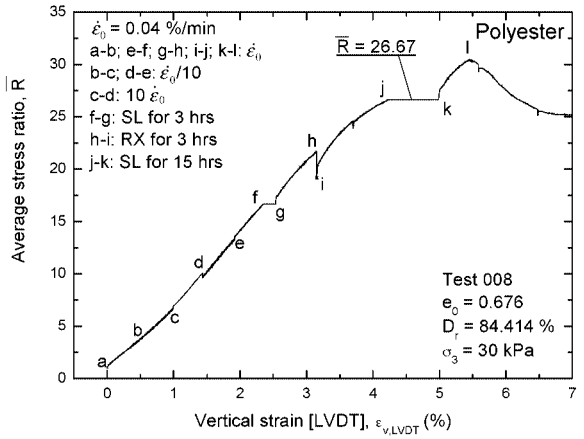

Fig. 25. $R-\varepsilon_{v,LVDT}$ **relation from a PSC test on a Toyoura sand specimen reinforced with a PET geogrid (test 008)**

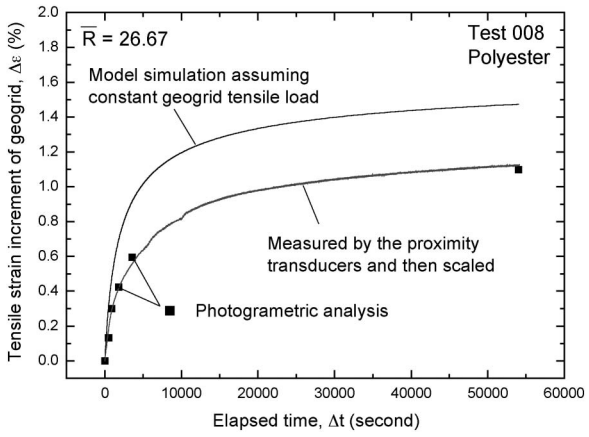

Fig. 26. Time history of measured tensile strain in a PET geogrid during sustained loading of a reinforced sand specimen at $\bar{R}=$ **26.67 (Fig. 25) and the one during sustained loading of the PET geogrid deduced by model simulation**

Sustained Loading Test on a PET Geogrid for 15 Hours (Test 008)

In order to investigate the geogrid behaviour during sustained loading of reinforced sand specimen at a state that is much closer to the failure state than the case present in Fig. 24, another test 008 was performed (*see* Table 1). In this test (Fig. 25), the specimen was PET geogrid-reinforced Toyoura sand and the strain rate was changed stepwise four times; sustained loading tests were performed at $\bar{R}=16.67$ for three hours and 26.67, close to the peak stress ratio, for 15 hours; and stress relaxation at $\bar{R}=21.67$ for three hours.

The deduced tensile load-tensile strain-time relation of a PET geogrid arranged in sand during the sustained loading at $\bar{R}=16.67$ in this test was similar to those presented in Fig. 24. The behaviour during the sustained loading at $\bar{R}=26.67$ was analysed additionally. Figure 26 shows the measured time history of tensile strain of the PET geogrid arranged in sand during the sustained loading of a reinforced sand specimen, obtained by the photogrametric method and the measurement of lateral strains of specimen. It may be seen that the tensile strain

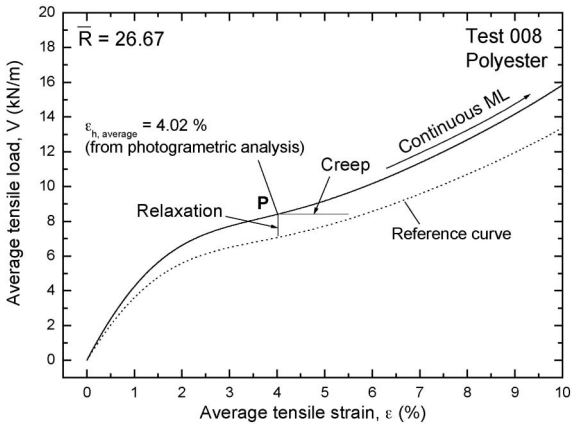

Fig. 27. Tensile load-strain relations of a PET geogrid subjected to three specified loading histories: continuous ML; 15-hour creep; and 15-hour load relaxation, obtained by model simulation for sustained loading of reinforced sand specimen at $\bar{R}=26.67$ **(Fig. 25)**

of the PET geogrid arranged in sand during the sustained loading of reinforced sand specimen is smaller than the one obtained by model simulation assuming that the tensile load in the PET geogrid is kept constant during the sustained loading. However, the difference between the two types of geogrid tensile strain is much smaller than the one seen in Fig. 13. This is due to a larger trend of creep deformation of the sand part during this sustained loading test at $\bar{R}=26.67$, resulting from the stress state of the reinforced sand specimen that was very close to its failure stress state.

Figure 27 shows the results from model simulations, similar to those presented in Fig. 18. The tensile load-strain relation for continuous ML at a strain rate of 0.054 %/min of the PET geogrid was obtained by model simulation. The strain rate was determined based on the geogrid strain increment from $\bar{R}=21.67$ to 26.67 obtained by the photogrametric analysis. The relations during: a) sustained loading at a fixed load; and b) load relaxation at a fixed strain, each lasting for 15 hours and both starting from point **P**, were obtained also by model simulation. At point **P**, $\bar{R}$ of the reinforced sand specimen is equal to 26.67 and the geogrid tensile strain obtained from the photogrametric analysis (n.b., similar to Fig. 12(a)) is 4.02%.

In the following, only the results obtained by the direct model simulation and the one deduced based on linear contours are presented. Figure 28 shows the measured time history of geogrid strain rate during the sustained loading at $\bar{R}=26.67$ and Fig. 29 shows the tensile load-tensile strain relation of the PET geogrid in sand during the sustained loading of reinforced sand specimen obtained by the direct model simulation based on the time history of geogrid strain rate presented in Fig. 28. Due to the fluctuation in the measured strain rate-time relation, the relation obtained by the direct model simulation presented in Fig. 29 exhibits a noticeable fluctuation. For this reason, the direct model simulation did not extend to elapsed times longer than 15 hours. In

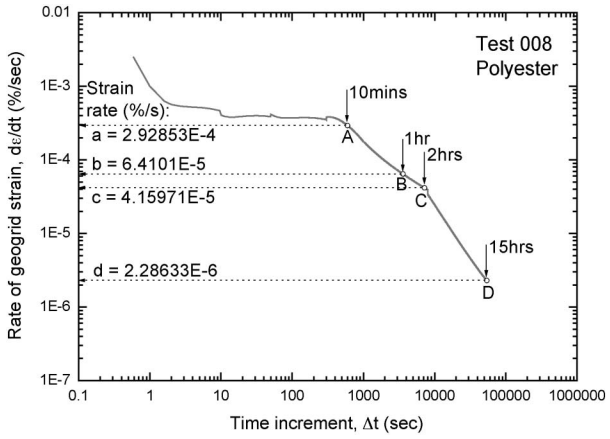

Fig. 28. Relationship between geogrid strain rate and elapsed time (full-log plot) from the fitted time history of strain increment of a PET geogrid arranged in sand during sustained loading of a reinforced sand specimen at $\bar{R} = 26.67$ presented in Fig. 26

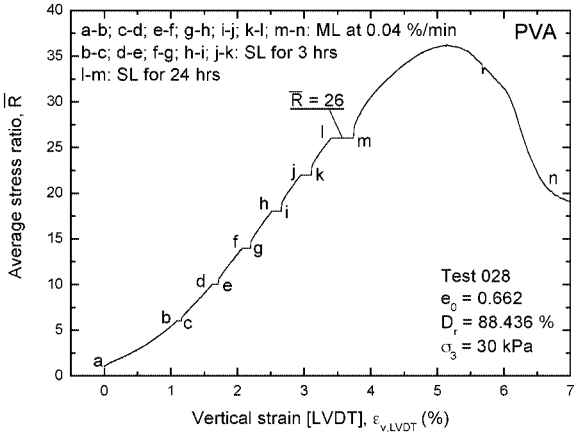

Fig. 30. $\bar{R} - \varepsilon_{v,LVDT}$ relation for sand reinforced with a PVA geogrid subjected to multi-stages of sustained loading during otherwise ML (test 028)

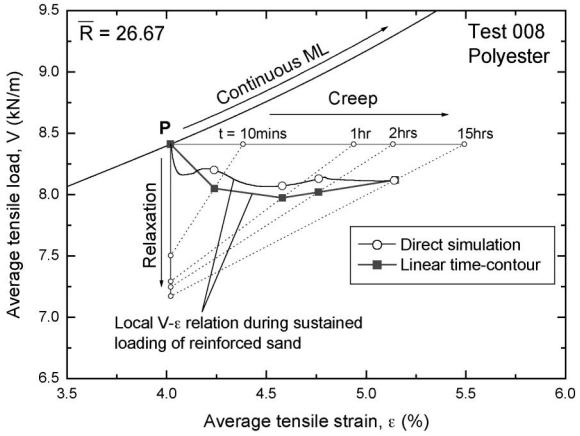

Fig. 29. Estimated tensile load-strain relation of a PET geogrid during the 15 hour-long sustained loading of reinforced sand at $\bar{R} = 26.67$ (Fig. 25)

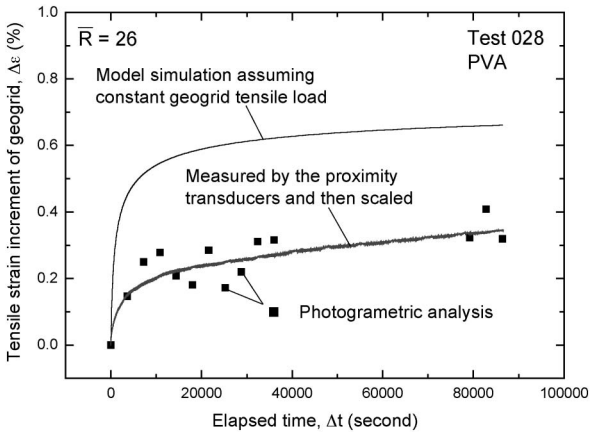

Fig. 31. Time history of measured tensile strain in a PVA geogrid during sustained loading of a reinforced sand specimen at $\bar{R} = 26$ (Fig. 30) and the one during sustained loading of the PVA geogrid deduced by model simulation

this figure, the tensile load-tensile strain relation obtained by the analysis based on the linear contours for the same elapsed times, similar to the one described in Fig. 20, is also presented. It may be seen that the general trends of behaviour of the two relations are very similar.

The trend of load-strain behaviour of the PET geogrid arranged in sand during the sustained loading of reinforced sand specimen at $\bar{R} = 26.67$ (Fig. 29) is generally similar to the one at $\bar{R} = 16.67$ (Fig. 24). However, the initial load reduction in this case (Fig. 29) is weaker. This trend of behaviour may be due to that the trend of creep deformation in the sand part of reinforced sand specimen is stronger because the stress state of the reinforced sand specimen at this sustained loading stage is closer to the failure state. In this case, the creep lateral tensile strain rate of the sand part is much higher than when $\bar{R}$ is lower, which induces positive lateral tensile strain increments in the geogrid, then increases the geogrid tensile load. Then, the possibility of creep rupture of geogrid in the long run is larger in this case than when the stress state is remote from the failure state.

Sustained Loading Test on a PVA Geogrid for 24 Hours (Test 028)

Lastly, the geogrid tensile load-strain-time behaviour during the sustained loading of PVA-reinforced Toyoura sand when the stress state of reinforced sand relative to the failure state is intermediate between the two cases described in the precedent sections is analysed. Figures 30, 31, 32, 33 and 34 show the results from the PSC test (test 028; Table 1) and analysis of the test data, similar to Figs. 9, 13, 15, 18 and 24. In this test, the specimen was subjected to five stages of sustained loading (each for three hours) and one stage of sustained loading for 24 hours during otherwise ML at constant strain rate of 0.04%/min. The sustained loading at $\bar{R} = 26$ was analysed.

Figure 31 shows the measured time history of geogrid tensile strain during the sustained loading for 24 hours of the reinforced sand specimen. Figure 32 shows the corresponding measured time history of geogrid strain rate. The continuous tensile load-tensile strain relations of the PVA geogrid shown in Fig. 33 was obtained by

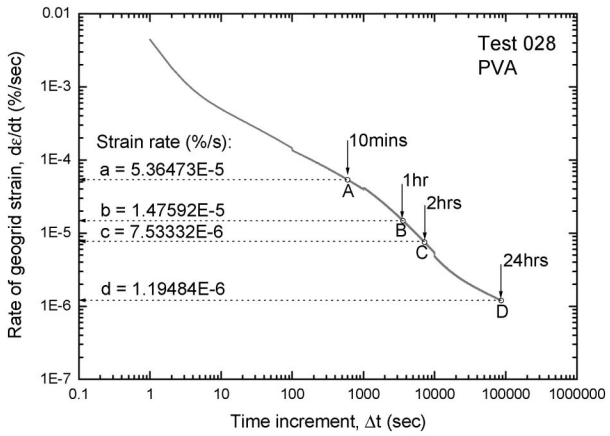

Fig. 32. Relationship between geogrid strain rate and elapsed time (full-log plot) from the fitted time history of strain increment of a PVA geogrid arranged in sand during sustained loading of a reinforced sand specimen presented in Fig. 31

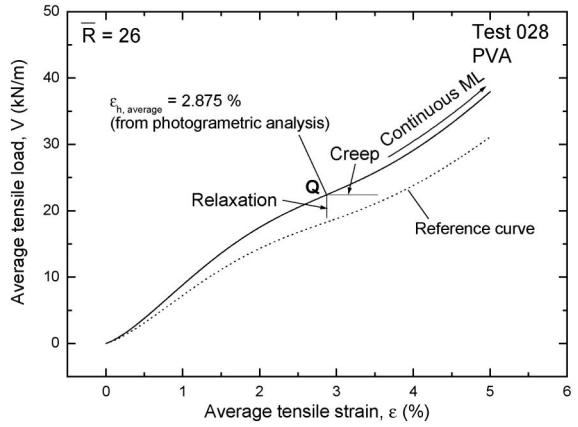

Fig. 33. Tensile load-strain relations of a PVA geogrid subjected to three specified loading histories: continuous ML; 24-hour creep; and 24-hour load relaxation, obtained by model simulation for sustained loading of a reinforced sand specimen at $\bar{R} = 26$ (Fig. 30)

model simulation of ML at a strain rate of 0.063%/min, which was determined based on the geogrid strain increment from $\bar{R} = 22$ to 26 during ML obtained by the photogrametric analysis. The parameters used in the model simulation are listed in Table 3. Figure 33 also shows the simulated tensile load-tensile strain relations of the PVA geogrid during sustained loading at a fixed load and load relaxation at a fixed strain, each lasting for 24 hours and both starting from point **Q** in the PSC test. At **Q**, $\bar{R}$ is equal to 26 and the geogrid tensile strain by the photogrametric analysis (n.b., similar to Fig. 12(a)) is 2.875%.

Figure 34 shows the four tensile load-strain-time relations of the PVA geogrid during the sustained loading of reinforced sand specimen at $\bar{R} = 26$, which were obtained by the direct model simulation; the linear contour method; the elastic spring-support model; and the isotach method, similar to Fig. 24. As the PVA geogrid has the isotach viscosity, the results from the direct model simulation and the isotach method should be the same. The linear contours for the same elapsed times are

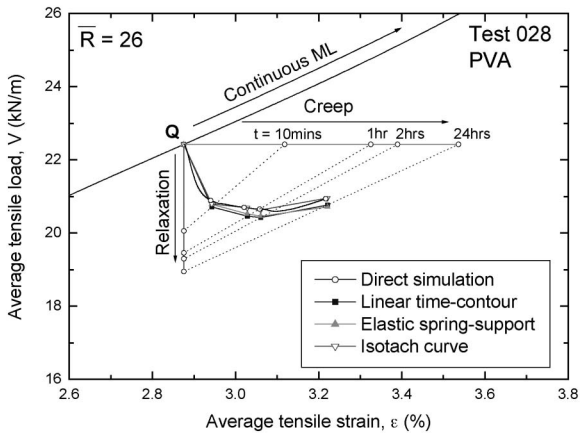

Fig. 34. Estimated tensile load-strain relation of a PVA geogrid during the 24 hour-long sustained loading of reinforced sand at $\bar{R} = 26$ (Fig. 30) obtained by the direct model simulation: the linear contour assumption, the elastic spring-support model, and the isotach curve

presented for reference. It may be seen from Fig. 34 that the relations deduced by the four methods are very similar. The general trends of behaviour seen from Fig. 34 are similar to those seen from Figs. 24 and 29.

Though the analysis performed in the present study is limited to those where failure is not imminent, the applicability of the non-linear three-component model is not limited by the level of stress. Tatsuoka et al. (2003) showed simulation of the creep failure of geomaterial by the non-linear three-component model. If the elasto-viscoplastic properties of a geogrid and the time histories of tensile strain of the geogrid during sustained loading of a reinforced sand specimen when failure is imminent become available, the model can simulate the tensile load-strain-time relation of the geogrid. The non-linear three-component model was applied only to one-dimensional cases in the present study. However, the model can be extended to analyse the two- or three-dimensional boundary value geotechnical engineering problems. For example, Siddiquee et al. (2006) incorporated this model into a Finite Element program code in order to analyse plane strain boundary value problems.

CONCLUSIONS

The following conclusions can be derived from the experimental results and their analysis described in this paper:

1) Significant creep deformation of geogrid-reinforced sand specimen was observed during sustained loading in drained plane strain compression. This can be attributed to the viscous properties of not only geogrid but also sand. The creep strain rate became more significant as the stress state became closer to the failure stress state.
2) The geogrid reinforced sand specimen exhibited very high stiffness for some stress range when monotonic loading (ML) was restarted at the original strain rate following the respective sustained loading. The

reinforced sand became stiffer and stronger during the subsequent ML towards the ultimate failure, which was due likely to the development of better interlocking between the geogrid and the adjacent sand during sustained loading. These results indicate that creep deformation of geogrid-reinforced sand is not a degrading phenomenon, but it is merely a result of interacting rate-dependent behaviours of sand and geogrid.

3) The restraining effects by the geogrid layers on the lateral deformation of sand specimen were clearly seen from local horizontal strain distributions constructed by photogrametric analysis.
4) The measured time histories of tensile strains of geogrid arranged in sand during sustained loading of reinforced sand specimen together with the results from numerical analysis of the test results by the non-linear three-component model indicated that the tensile load mobilised in the geogrid arranged in the sand specimen decreased with time during sustained loading of reinforced sand specimen at fixed boundary stress conditions. The load reduction was larger when the stress state during the sustained loading was more remote from the failure stress state of reinforced sand.

The last conclusion suggests that it is conservative to assume that the tensile load in the geogrid reinforcement arranged in the full-scale backfill subjected to constant working loads is always maintained constant. It is also suggested that, when designed using the design tensile strength of reinforcement determined by taking into account a number of reduction factors as well as an overall safety factor (Fig. 1), it is unlikely that ordinary GRS structures fail by creep rupture of the geosynthetic reinforcement under typical static working conditions, in particular when seismic load is taken into account in the structural design.

ACKNOWLEDGEMENTS

This study was supported by the Japan Society for the Promotion of Science through the grant: ''Advanced application of soil reinforcement technology to highly-earthquake-resistant reinforcement of existing soil structures and construction of highly-earthquake resistant and environment-friendly soil structures''.

REFERENCE

1) Alshibli, K. A. and Sture, S. (2000): Shear band formation in plane strain compression, *J. Geotech. Geoenviron. Engrg.*, **126**(6), 495–503.
2) Cook, R. D., Malkus, D. S. and Plesha, M. E. (1989): *Concepts and Applications of Finite Element Analysis, 3rd Edition*, John Wiley & Sons, Inc.
3) Desrues, J. (1984): La localisation de la deformation dans les materiaux granulaires, *These de Doctorate es Science*, Universite Scientifique et Medicale de Grenoble, France.
4) Di Benedetto, H., Sauzéat, C. and Geoffroy, H. (1999): Modelling viscous effects for sand and behaviour in the small strain domain, *Proc. 2nd Int. Symp. on Pre-failure Deformation Characteristics of Geomaterials, IS Torino*, (eds. by Jamiolkowski et al.), Panel Presentation, Balkema, **2**, 1357–1367.
5) Di Benedetto, H., Tatsuoka, F. and Ishihara, M. (2002): Time-dependent shear deformation characteristics of sand and their constitutive modelling, *Soils and Foundations*, **42**(2), 1–22.
6) Hirakawa, D., Uchimura, T., Shibata, Y. and Tatsuoka, F. (2002): Time-dependant deformation of geosynthetics and geosynthetic-reinforced soil structures, *Proc. 7th Int. Conf. Geosynthetics*, Nice, **4**, 1427–1430.
7) Hirakawa, D., Kongkitkul, W., Tatsuoka, F. and Uchimura, T. (2003): Time-dependent stress-strain behaviour due to viscous properties of geogrid reinforcement, *Geosynthetics Int.*, **10**(6), 176–199.
8) Hirakawa, D., Takaoka, H., Tatsuoka, F. and Uchimura, T. (2004): Deformation characteristics of geosynthetics retaining wall loaded on the crest, *Proc. 3rd Asian Regional Conf. Geosynthetics (GeoAsia 2004)*, Seoul, 240–247.
9) Huang, C.-C. and Tatsuoka, F. (1990): Bearing capacity of reinforced horizontal sandy ground, *Geotextiles and Geomembranes*, **9**(1), 51–82.
10) Huang, C.-C. and Tatsuoka, F. (1994): Stability analysis for footings on reinforced sand slopes, *Soils and Foundations*, **34**(3), 21–37.
11) Huang, C.-C., Tatsuoka, F. and Sato, Y. (1994): Failure mechanisms of reinforced sand slopes loaded with a footing, *Soils and Foundations*, **34**(2), 27–40.
12) Kiyota, T. and Tatsuoka, F. (2006): Viscous property of loose sand in triaxial compression, extension and cyclic loading, *Soils and Foundations*, **46**(5), 665–684.
13) Kongkitkul, W. (2004): Effects of material viscous properties on the residual deformation of geosynthetic-reinforced sand, *Ph.D. Thesis*, University of Tokyo, 658.
14) Kongkitkul, W., Hirakawa, D., Tatsuoka, F. and Uchimura, T. (2004): Viscous deformation of geosynthetic reinforcement under cyclic loading conditions and its model simulation, *Geosynthetics Int.*, **11**(2), 73–99.
15) Kongkitkul, W., Hirakawa, D. and Tatsuoka, F. (2007a): Viscous behaviour of geogrids; experiment and simulation, *Soils and Foundations*, **47**(2), 265–283.
16) Kongkitkul, W., Tatsuoka, F. and Hirakawa, D. (2007b): Effects of reinforcement type and loading history on the deformation of reinforced sand in plane strain compression, *Soils and Foundations*, **47**(2), 395–414.
17) Kongkitkul, W., Tatsuoka, F. and Hirakawa, D. (2007c): Creep rupture curve for simultaneous creep deformation and degradation of geosynthetic reinforcement, *Geosynthetics Int.*, **14**(4), (accepted).
18) Kotake, N., Tatsuoka, F., Tanaka, T., Siddiquee, M. S. A. and Yamauchi, H. (1999): An insight into the failure of reinforced sand in plane strain compression by FEM simulation, *Soils and Foundations*, **39**(5), 103–130.
19) Kotake, N., Tatsuoka, F., Tanaka, T., Siddiquee, M. S. A. and Huang, C.-C. (2001a): Effects of tensile and bending rigidities of reinforcement in reinforcing soil structures and ground, *Proc. IS Kyushu*, (eds. by Ochiai et al.), Balkema, **1**, 571–576.
20) Kotake, N., Tatsuoka, F., Tanaka, T., Siddiquee, M. S. A. and Huang, C.-C. (2001b): FEM simulation of the bearing capacity of level reinforced ground subjected to footing load, *Geosynthetics Int.*, **8**(6), 501–549.
21) Kotake, N., Tatsuoka, F., Tanaka, T., Siddiquee, M. S. A. and Huang, C.-C. (2004): FEM simulation of the failure of reinforced sand slopes subjected to footing load, *Geosynthetics Int.*, **11**(1), 1–18.
22) Liang, L., Saada, A., Figueroa, J. L. and Cope, C. T. (1997): The use of digital image processing in monitoring shear band development, *Geotech. Test. J.*, **20**(3), 324–339.
23) Ling, H.-I. and Tatsuoka, F. (1994): Performance of anisotropic geosynthetic-reinforced cohesive soil mass, *J. Geotech. Engrg.*, ASCE, **120**(7), 1166–1184.
24) Matsushita, M., Tatsuoka, F., Koseki, J., Cazacliu, B., Di Benedetto, H. and Yasin, S. J. M. (1999): Time effects on the pre-

peak deformation properties of sands, *Proc. 2nd Int. Conf. Pre-Failure Deformation Characteristics of Geomaterials, IS Torino '99* (eds. by Jamiolkowski et al.), Balkema, Rotterdam, **1**, 681–689.
25) Nawir, H., Tatsuoka, F. and Kuwano, R. (2003): Experimental evaluation of the viscous properties of sand in shear, *Soils and Foundations*, **43**(6), 13–31.
26) Peng, F.-L., Kotake, N., Tatsuoka, F., Hirakawa, D. and Tanaka, T. (2000): Plane strain compression behaviour of geogrid-reinforced sand and its numerical analysis, *Soils and Foundations*, **40**(3), 55–74.
27) Roh, H.-S. and Tatsuoka, F. (2002): Effects of preloading and prestressing on the strength and stiffness of geosynthetic-reinforced clay in plane strain compression, *Geosynthetics Int.*, **8**(5), 393–444.
28) Santucci de Magistris, F., Koseki, J., Amaya, M., Hamaya, S., Sato, T. and Tatsuoka, F. (1999): A triaxial testing system to evaluate stress-strain behaviour of soils for wide range of strain and strain rate, *Geotech. Test. J.*, **22**(1), 44–60.
29) Shinoda, M., Horii, K., Bathurst, R. and Tatsuoka, F. (2002): Investigation of tensile strength after creep and stress relaxation of geogrids, *Proc. 37th Japan Nat. Conf. Geotech. Engrg.*, Japanese Geotechnical Society, Osaka, 773–774 (in Japanese).
30) Shinoda, M., Uchimura, T. and Tatsuoka, F. (2003): Increasing the stiffness of mechanically reinforced backfill by preloading and prestressing, *Soils and Foundations*, **43**(1), 75–92.
31) Siddiquee, M. S. A., Tatsuoka, F. and Tanaka, T. (2006): FEM simulation of the viscous effects on the stress-strain behaviour of sand in plane strain compression, *Soils and Foundations*, **46**(1), 99–108.
32) Stroud, M. A. (1971): The behavior of sand at low stress levels in the simple shear apparatus, *Ph.D. Thesis*, University of Cambridge, Cambridge, UK.
33) Tatsuoka, F. and Yamauchi, H. (1986): A reinforcing method for steep clay slopes with a non-woven fabric, *Geotextiles and Geomembranes,* **4**(3/4), 241–268.
34) Tatsuoka, F., Sato, T., Park, C.-S., Kim, Y.-S., Mukabi, J. N. and Kohata, Y. (1994): Measurements of elastic properties of geomaterials in laboratory compression tests, *Geotech. Test. J.*, **17**(1), 80–94.
35) Tatsuoka, F., Tateyama, M., Uchimura, T. and Koseki, J. (1997): Geosynthetics reinforced soil retaining walls as important permanent structures, 1996–1997 Mercer Lecture, *Geosynthetics Int.*, **4**(2), 81–136.
36) Tatsuoka, F., Santucci de Magistris, F., Momoya, F. and Maruyama, N. (1999): Isotach behaviour of geomaterials and its modelling, *Proc. 2nd Int. Conf. Pre-failure Deformation Characteristics of Geomaterials, Torino, 1999* (eds. by Jamiolkowski et al.), Balkema, **1**, 491–499.
37) Tatsuoka, F., Ishihara, M., Di Benedetto, H. and Kuwano, R. (2002): Time-dependent shear deformation characteristics of geomaterials and their simulation, *Soils and Foundations*, **42**(2), 103–129.
38) Tatsuoka, F., Di Benedetto, H. and Nishi, T. (2003): A framework for modelling of the time effects on the stress-strain behaviour of geomaterials, *Proc. 3rd Int. Sym. Deformation Characteristics of Geomaterials, IS Lyon 03* (eds. by Di Benedetto et al.), Balkema, September 2003, 1135–1143.
39) Tatsuoka, F., Hirakawa, D., Shinoda, M., Kongkitkul, W. and Uchimura, T. (2004): An old but new issue; viscous properties of polymer geosynthetic reinforcement and geosynthetic-reinforced soil structures, Keynote Lecture, *Proc. 3rd Asian Reg. Conf. Geosynthetics (GeoAsia 2004)*, Seoul, 29–77.
40) Tatsuoka, F., Kongkitkul, W. and Hirakawa, D. (2006): Viscous property and time-dependent degradation of geosynthetic reinforcement, *Proc. 8th Int. Conf. Geosynthetics* (eds. by Kuwano and Koseki), Yokohama, Japan, **4**, 1587–1590.
41) Uchimura, T., Tateyama, M., Tanaka, I. and Tatsuoka, F. (2003): Performance of a preloaded-prestressed geogrid-reinforced soil pier for a railway bridge, *Soils and Foundations*, **43**(6), 155–172.
42) Yoshida, T., Tatsuoka, F., Siddiquee, M. S. A., Kamegi, Y. and Park, C.-S. (1994): Shear banding in sands observed in plane strain compression, *Proc. 3rd Int. Workshop on Localisation and Bifurcation Theory for Soils and Rocks* (eds. by Chambon et al.), Grenoble (Aussois), France, Balkema, Rotterdam, 165–179.
43) Yoshida, T. and Tatsuoka, F. (1997): Deformation property of shear band in sand subjected to plane strain compression and its relation to particle characteristics, *Prof. 14th ICSMFE* (ed. by Publications Committee of XIV ICSMFE), Hamburg, Germany, 237–240.

APPENDIX A: LOCAL STRAIN CALCULATION

Isoparametric Formulation

Referring to Fig. 7, for a single four-node element, the local coordinate (ξ, η) of any point within the element can be mapped or transformed to global Cartesian coordinates (x, y) by:

$$x(\xi, \eta) = \sum_{i=1}^{4} N_i(\xi, \eta) \cdot x_i \tag{A1a}$$

$$y(\xi, \eta) = \sum_{i=1}^{4} N_i(\xi, \eta) \cdot y_i \tag{A1b}$$

where (x_i, y_i) are the Cartesian coordinates of four nodes forming an element and $N_i(\xi, \eta)$ is the shape function, which is defined as:

$$N_i(\xi, \eta) = \frac{1}{4}(1 + \xi_i \cdot \xi)(1 + \eta_i \cdot \eta) \tag{A2}$$

where (ξ_i, η_i) represents the coordinates of the respective four nodes in the natural coordinate system.

Strains are calculated in terms of a field variable ϕ and its derivatives $\partial\phi/\partial x$ and $\partial\phi/\partial y$. In this study, the field variables ϕ are displacement scalars u and v in x (i.e., horizontal) and y (i.e., vertical) directions, respectively. The displacement scalars u and v at each node i ($i = 1$, 2, 3, 4) of the respective element were calculated as:

$$u_i = x_i - (x_i)_{\text{initial}} \tag{A3a}$$

$$v_i = y_i - (y_i)_{\text{initial}} \tag{A3b}$$

where (x_i, y_i) are the coordinates of node i at an instant t; and $(x_i, y_i)_{\text{initial}}$ are the coordinates of node i at the start of shearing the reinforced PSC specimen.

For isoparametric elements, the shape function representing the field variables, $[N]$, and the one representing geometries (coordinates), $[\tilde{N}]$, are identical. Therefore, any field variable can be expressed by using the same shape function as:

$$\phi(\xi, \eta) = \sum_{i=1}^{4} N_i(\xi, \eta) \cdot \phi_i \tag{A4}$$

and its derivative with respect to x and y is given as:

$$\frac{\partial\phi}{\partial x} = \sum_{i=1}^{4} \frac{\partial N_i}{\partial x} \cdot \phi_i \tag{A5a}$$

$$\frac{\partial\phi}{\partial y} = \sum_{i=1}^{4} \frac{\partial N_i}{\partial y} \cdot \phi_i \tag{A5b}$$

The derivatives of the shape function with respect to x and y can be determined as:

$$\begin{bmatrix} \frac{\partial N_i}{\partial x} \\ \frac{\partial N_i}{\partial y} \end{bmatrix} = \begin{bmatrix} \frac{\partial x}{\partial \xi} & \frac{\partial y}{\partial \xi} \\ \frac{\partial x}{\partial \eta} & \frac{\partial y}{\partial \eta} \end{bmatrix}^{-1} \cdot \begin{bmatrix} \frac{\partial N_i}{\partial \xi} \\ \frac{\partial N_i}{\partial \eta} \end{bmatrix} = [J]^{-1} \cdot \begin{bmatrix} \frac{\partial N_i}{\partial \xi} \\ \frac{\partial N_i}{\partial \eta} \end{bmatrix}$$

$$= \frac{1}{|J|} \cdot \begin{bmatrix} J_{22} & -J_{12} \\ -J_{21} & J_{11} \end{bmatrix} \cdot \begin{bmatrix} \frac{\partial N_i}{\partial \xi} \\ \frac{\partial N_i}{\partial \eta} \end{bmatrix} \quad \text{(A6)}$$

where $[J]^{-1}$ is the *inverse* of ''Jacobian'' matrix $[J]$; and $|J| = J_{11} \cdot J_{22} - J_{12} \cdot J_{21}$ is the determinant of the Jacobian matrix.

Strains were calculated at the *centre* of each element where $(\xi, \eta) = (0, 0)$. By knowing coordinates x and y at the four nodes of each formed element, the Jacobian matrix of the respective element can be determined by following Eqs. (A1) and (A2). Subsequently, the derivatives of the shape function with respect to x and y can be calculated by following Eq. (A6).

Calculation of Strain Values

Following the continuum theory, the following equations are derived to calculate the values of strain:

Horizontal strain (positive in compression):

$$\varepsilon_x = -\frac{\partial u}{\partial x} = -\sum_{i=1}^{4} \frac{\partial N_i(\xi, \eta)}{\partial x} \cdot u_i \quad \text{(A7)}$$

Vertical strain (positive in compression):

$$\varepsilon_y = -\frac{\partial v}{\partial y} = -\sum_{i=1}^{4} \frac{\partial N_i(\xi, \eta)}{\partial y} \cdot v_i \quad \text{(A8)}$$

Orthogonal shear strain:

$$\gamma_{xy} = -\left[\frac{\partial u}{\partial y} + \frac{\partial v}{\partial x} \right] = -\left[\sum_{i=1}^{4} \frac{\partial N_i(\xi, \eta)}{\partial y} \cdot u_i + \sum_{i=1}^{4} \frac{\partial N_i(\xi, \eta)}{\partial x} \cdot v_i \right] \quad \text{(A9)}$$

Major principal strain:

$$\varepsilon_1 = \frac{1}{2}(\varepsilon_x + \varepsilon_y) + \sqrt{\frac{1}{4}(\varepsilon_x - \varepsilon_y)^2 + \left(\frac{\gamma_{xy}}{2} \right)^2} \quad \text{(A10)}$$

Minor principal strain:

$$\varepsilon_3 = \frac{1}{2}(\varepsilon_x + \varepsilon_y) - \sqrt{\frac{1}{4}(\varepsilon_x - \varepsilon_y)^2 + \left(\frac{\gamma_{xy}}{2} \right)^2} \quad \text{(A11)}$$

Maximum shear strain:

$$\gamma_{max} = \varepsilon_1 - \varepsilon_3 \quad \text{(A12)}$$

Volumetric strain (positive in compression; n.b., $\varepsilon_2 \equiv 0$):

$$\varepsilon_{vol} = \varepsilon_1 + \varepsilon_3 \quad \text{(A13)}$$

APPENDIX B: NON-LINEAR THREE-COMPONENT MODEL

In the framework of the non-linear three-component model developed for geosynthetic reinforcement (Fig. 17; Hirakawa et al., 2003; Kongkitkul et al., 2007a), the tensile load, V, consists of inviscid and viscous components, V^f and V^v, while the tensile strain rate, $\dot{\varepsilon}$, consists of elastic and irreversible components, $\dot{\varepsilon}^e$ and $\dot{\varepsilon}^{ir}$. The following four different types of V^v were proposed to simulate the viscous properties of a wide variety of geosynthetic reinforcement:

Isotach viscosity: The current value of V^v is a unique function of irreversible tensile strain, ε^{ir}, and its rate, $\dot{\varepsilon}^{ir}$, as long as ML continues, while the change in the V^v value upon a change in $\dot{\varepsilon}^{ir}$ is persistent with an increase in ε^{ir}. Therefore, the tensile load-strain curves for ML at different constant strain rates are separated from each other and the separation increases with an increase in V^f. Therefore, V^v can be written as:

$$V^v(\varepsilon^{ir}, \dot{\varepsilon}^{ir}) = V^v_{iso}(\varepsilon^{ir}, \dot{\varepsilon}^{ir}) = V^f(\varepsilon^{ir}) \cdot g_v(\dot{\varepsilon}^{ir}) \quad \text{(B1)}$$

where $g_v(\dot{\varepsilon}^{ir})$ is the viscosity function, for which the following non-linear function has been proposed for geomaterial (Di Benedetto et al., 2002; Tatsuoka et al., 2002):

$$g_v(\dot{\varepsilon}^{ir}) = g_{v1}(\dot{\varepsilon}^{ir}) = \alpha \cdot [1 - \exp\{1 - (|\dot{\varepsilon}^{ir}| / \dot{\varepsilon}^{ir}_r + 1)^m\}] \quad \text{(B2)}$$

where $|\dot{\varepsilon}^{ir}|$ is the absolute value of $\dot{\varepsilon}^{ir}$; α, m and $\dot{\varepsilon}^{ir}_r$ are the positive material constants. On the other hand, Di Benedetto et al. (1999) chose the following function for $g_v(\dot{\varepsilon}^{ir})$:

$$g_v(\dot{\varepsilon}^{ir}) = g_{v2}(\dot{\varepsilon}^{ir}) = \alpha^* \cdot (\dot{\varepsilon}^{ir} / \dot{\varepsilon}^{ir}_0)^{1+b^*} \quad \text{(B3)}$$

where: α^*, b^* and $\dot{\varepsilon}^{ir}_0$ are constants. It can be shown that the two expressions, Eqs. (B2) and (B3), provide nearly the same evolutions for a wide range of positive value of $\dot{\varepsilon}^{ir}$ and the parameters, while differences become noticeable only at very small or very large values of $\dot{\varepsilon}^{ir}$. Kongkitkul et al. (2007a) proposed to combine Eqs. (B2) and (B3) so that Eq. (B2) is fitted to the data when the encountered $\dot{\varepsilon}^{ir}$ values are relatively high and Eq. (B3) when the encountered $\dot{\varepsilon}^{ir}$ values were relatively low. In the present study, this modification was also introduced as precisely as possible to simulate the tensile load-strain-time behaviour of a geogrid arranged in sand subjected to drained PSC. Hirakawa et al. (2003) and Kongkitkul et al. (2007a) showed that the isotach type viscosity is relevant to the PVA geogrid as well as the other geosynthetic reinforcement types they tested, except for the PET geogrid.

TESRA viscosity: The current value of V^v is a function of not only the instantaneous values of ε^{ir} and $\dot{\varepsilon}^{ir}$, but also recent loading history even in the case of ML, while a change in the V^v value by an increment, $d\varepsilon^{ir}$, and a change in $\dot{\varepsilon}^{ir}$ decays with an increase in ε^{ir}. Therefore, the tensile load-tensile strain relations for ML at different constant strain rates tend to collapse into a single relation. The decay behaviour of V^v is called the TESRA viscosity, which can be expressed as:

$$V^v = V^v_{TESRA}(\varepsilon^{ir}, \dot{\varepsilon}^{ir}, h_S) = \int_{\tau=\varepsilon^{ir}_1}^{\varepsilon^{ir}} [dV^v_{iso}]_{(\tau)} \cdot r_1^{(\varepsilon^{ir}-\tau)} \quad \text{(B4)}$$

where ε^{ir} is the current irreversible strain, ε^{ir}_1 is the irreversible strain at the start of loading where the viscous effect

is zero ($\varepsilon_1^{ir}=0$ in the present case); V_{iso}^{v} is the isotach viscosity load component obtained from Eq. (B1); and τ is the irreversible strain at which the viscous load increment $[dV_{iso}^{v}]_{(\tau)}$ takes place. The function $r_1^{(\varepsilon^{ir}-\tau)}$ is called the decay function. As r_1 is a positive constant lower than unity, $r_1^{(\varepsilon^{ir}-\tau)}$ decreases with an increase in the strain difference, $\varepsilon^{ir}-\tau$. In this way, the current value of V_{TESRA}^{v} (when $\varepsilon^{ir}=\varepsilon^{ir}$) becomes dependent of the recent history of ε^{ir}. When $r_1=1.0$, V_{TESRA}^{v} (Eq. (B4)) becomes the same as V_{iso}^{v} (Eq. (B1)).

General TESRA viscosity: Like the TESRA type viscosity, a change in the V^{v} value that has taken place by an increment, $d\varepsilon^{ir}$, and/or a change in $\dot{\varepsilon}^{ir}$ decays with an increase in ε^{ir}, but the decay rate increases with an increase in ε^{ir}, the viscosity type changing from the isotach type at small strains towards the TESRA type at large strains. Then, Eq. (B4) is modified to:

$$V^{v}=V_{G.TESRA}^{v}=\int_{\tau=\varepsilon_f^{ir}}^{\varepsilon^{ir}}[dV_{iso}^{v}]_{(\tau)}\cdot[r(\varepsilon^{ir})]^{(\varepsilon^{ir}-\tau)} \quad (B5)$$

where $[r(\varepsilon^{ir})]^{(\varepsilon^{ir}-\tau)}$ is the decay function; and $r(\varepsilon^{ir})$ is the parameter that decreases with ε^{ir}. Tatsuoka et al. (2002) proposed the following:

At $\varepsilon^{ir}=0$:

$r(\varepsilon^{ir})=r_i$ (positive and equal to or smaller than unity) (B6a)

For $0<\varepsilon^{ir}<c$:

$$r(\varepsilon^{ir})=\frac{r_i+r_f}{2}+\frac{r_i-r_f}{2}\cdot\cos\left[\pi\cdot\left(\frac{\varepsilon^{ir}}{c}\right)^{n}\right] \quad (B6b)$$

For $\varepsilon^{ir}\geq c$:

$r(\varepsilon^{ir})=r_f$ (positive and smaller than r_i) (B6c)

where: r_i, r_f, c and n are material constants.

When $r(\varepsilon^{ir})\equiv r_i\equiv r_f$ is constant and lower than unity, Eq. (B5) returns to Eq. (B4).

Combined viscosity: V^{v} consists of the isotach and general TESRA viscous components as:

$$V^{v}(\varepsilon^{ir},\dot{\varepsilon}^{ir},h_s)=\lambda^{v}\cdot V_{iso}^{v}(\varepsilon^{ir},\dot{\varepsilon}^{ir})+(1-\lambda^{v})\cdot V_{G.TESRA}^{v}(\varepsilon^{ir},\dot{\varepsilon}^{ir},h_s) \quad (B7)$$

where λ^{v} is the material constant between zero and unity with polymer geosynthetic reinforcement. Equation (B7) can be rewritten as:

$$V^{v}(\varepsilon^{ir},\dot{\varepsilon}^{ir},h_s)=\int_{\tau=\varepsilon_f^{ir}}^{\varepsilon^{ir}}[dV_{iso}^{v}]_{(\tau)}\cdot g_{decay.general}(\varepsilon^{ir}-\tau) \quad (B8a)$$

$$g_{decay.general}(\varepsilon^{ir}-\tau)=\lambda^{v}+(1-\lambda^{v})\cdot[r(\varepsilon^{ir})]^{(\varepsilon^{ir}-\tau)} \quad (B8b)$$

where $g_{decay.general}(\varepsilon^{ir}-\tau)$ is the generalised decay function.

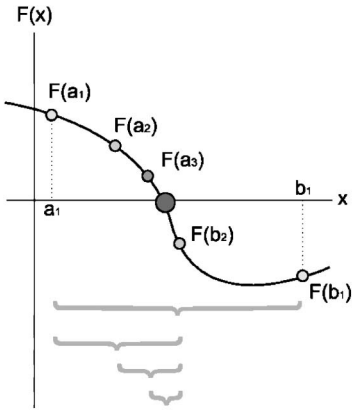

Fig. C1. Illustration of a few steps of the bisection method applied over an initial range [a1; b1]: The largest circle denotes the root of the function (after Wikipedia, the free encyclopedia)

When λ^{v} is equal to 1.0 and 0.0, Eqs. (B7) or (B8) returns to, respectively, Eqs. (B1) (the isotach viscosity) and (B5) (the general TESRA viscosity). This is the most flexible type while including the three types above. Hirakawa et al. (2003) and Kongkitkul et al. (2007a) showed that this type of viscosity is relevant to the PET geogrid and was also used in the present study.

APPENDIX C: ITERATION METHOD USED IN MODEL SIMULATION

Simulations by the non-linear three-component model presented in this paper were performed by a method of iteration to find the root (i.e., the solution) for respective steps of a very small time increment. The iteration was done following the bisection method, a root-finding algorithm which works by repeatedly dividing an interval in half and then selecting the subinterval in which the root exists (Fig. C1).

Suppose that we want to solve Eq. $f(x)=0$. Giving two points a and b such that $f(a)$ and $f(b)$ have opposite signs, we know by the intermediate value theorem that, as long as $f(x)$ is continuous, $f(x)$ must have at least one root within the range $[a, b]$. The bisection method divides the interval into two by computing $c=(a+b)/2$. There are now two possibilities: either $f(a)$ and $f(c)$ have opposite signs, or $f(c)$ and $f(b)$ have opposite signs. The bisection algorithm is then applied to a sub-interval where the sign change occurs, taking advantage of that the bisection algorithm is inherently recursive. In the simulations presented in this paper, when $|f(x)|<10^{-7}$, x was considered to be the root.